J. Fluid Mech. (2003), *vol.* 483, *pp.* 199–223. © 2003 Cambridge University Press
DOI: 10.1017/S0022112003004191 Printed in the United Kingdom

Vertical velocity in mesoscale geophysical flows

By ÁLVARO VIÚDEZ† AND DAVID G. DRITSCHEL

School of Mathematics and Statistics, University of St Andrews, St Andrews, UK

(Received 15 February 2002 and in revised form 12 September 2002)

An analysis of the vertical velocity field using the full generalized omega equation (ω-equation) in a single mesoscale baroclinic oceanic gyre is carried out. The evolution of the gyre over 20 inertial periods is simulated using a new three-dimensional numerical model which directly integrates the horizontal ageostrophic vorticity, explicitly conserves the potential vorticity (PV) via contour advection on isopycnal surfaces, and inverts the nonlinear PV definition via the solution of a three-dimensional Monge–Ampère equation. In this framework the ω-equation comes simply from the horizontal divergence of the horizontal ageostrophic vorticity prognostic equation. The ageostrophic vorticity is written as the Laplacian of a vector potential $\boldsymbol{\varphi}$, from which both the velocity and the density fields are recovered, respectively, from the curl and divergence of $\boldsymbol{\varphi}$. A new initialization technique based on the slow, progressive growth of the PV field during an initial time interval is used to avoid the generation of internal gravity waves during the initialization of the gyre. This method generates a nearly balanced baroclinic gyre for which the influence of internal gravity waves in the mesoscale vertical velocity field is negligible.

The numerical fields obtained are then used to carry out a first numerical analysis of the ω-equation. The analysis shows that, for moderately high Rossby numbers, the local and the advective rates of change of the differential ageostrophic vertical vorticity (ζ_z') are of the same order of magnitude as the three largest terms in the ω-equation. There is, however, a large cancellation between these two terms, resulting in the approximate material conservation of ζ_z'. This might explain the 'over-applicability' of the quasi-geostrophic (QG) ω-equation for Rossby numbers larger than 0.1. The QG vertical velocity is only 22% smaller than the total vertical velocity for the case studied (having a Rossby number of -0.5).

1. Introduction

Mesoscale geophysical flows are nearly tangential to surfaces of constant geopotential, that is, they are dominantly 'horizontal'. In the ocean, horizontal velocities are about a factor 10^4 larger than the cross-geopotential, or vertical, velocities.

The mesoscale vertical velocity, though small in comparison with the horizontal velocity, is also important for the marine ecosystem, since it is able to transport upward tens of metres of oceanic waters rich in nutrients from the dark deeper layers to the photic zone. But direct experimental measurements of mesoscale vertical velocities are difficult to carry out and instead a number of indirect methods have been developed to estimate these velocities (originally for atmospheric applications,

† Present address: Institut de Ciènces del Mar, P. Maritim 37, Barcelona, Spain.

https://doi.org/10.1017/S0022112003004191 Published online by Cambridge University Press

see Panofsky 1946). Perhaps the most successful method consists of obtaining the quasi-geostrophic (QG) vertical velocity (w^q) from a known density field ρ via the QG 'omega equation' (hereafter, the ω^q-equation). The ω^q-equation (see e.g. Holton 1992, § 6.4) is a three-dimensional linear equation of the form $L^q\{w^q\} = \mathscr{R}^q\{\rho\}$ where, in Cartesian coordinates, the linear operator $L^q \equiv c^2\nabla_h^2 + \partial_z^2$ is proportional to the QG Laplacian operator, $c \equiv N/f$ is the ratio of a given mean buoyancy frequency, N, to a given mean inertial frequency, f, $\nabla_h = (\partial_x, \partial_y)$ is the horizontal gradient, and on the right-hand side $\mathscr{R}^q$ is a known function of ρ.

Originally, the ω^q-equation was derived by eliminating the local rate of change of differential geostrophic vertical vorticity ζ_z^g between the horizontal momentum and mass conservation equations under the QG approximation. Let $\boldsymbol{u} = (u, v, w)$ denote the three-dimensional velocity, and $\boldsymbol{\omega} = \operatorname{curl}\boldsymbol{u} = (\xi, \eta, \zeta)$ and $\boldsymbol{\omega}^a = \operatorname{curl}\boldsymbol{u} + f\boldsymbol{k}$ denote the three-dimensional relative and absolute vorticity, respectively. In that original formulation, (see e.g. Holton 1992, § 6.4) the function $\mathscr{R}^q$ involves two terms, namely the differential geostrophic advection of geostrophic vertical vorticity $(\boldsymbol{u}_h^g \cdot \nabla_h \zeta^g)_z$ and the Laplacian of the geostrophic advection of density $\nabla_h^2(\boldsymbol{u}_h^g \cdot \nabla_h \rho)$. However, there is a large cancellation between these two terms (e.g. Trenberth 1978) since they both include, with opposite signs, the geostrophic advection of differential geostrophic vorticity $\boldsymbol{u}_h^g \cdot \nabla_h \zeta_z^g$. This ω^q-equation is referred to here as the *advective* ω^q-equation. Later, Hoskins, Draghici & Davies (1978) realized that $\mathscr{R}^q$ could be written as $2\nabla_h \cdot \boldsymbol{Q}_h^g$, where the geostrophic vector $\boldsymbol{Q}_h^g$ is proportional to $\nabla_h \boldsymbol{u}_h^g \cdot \nabla_h \rho$. This formulation avoids the cancellation of terms and led to a new interpretation of the ω^q-equation, known as the $\boldsymbol{Q}$-vector ω^q-equation. In a numerical study, Strass (1994) concluded that the pattern of the modelled w was better diagnosed using the divergence of $\boldsymbol{Q}^g$ than using the isopycnic advection and vorticity advection equations.

Subsequent studies in dynamic meteorology extended the advective ω^q-equation beyond the QG approximation with the formulation and analysis of the *generalized* advective ω-equation (Krishnamurti 1968; Pauley & Nieman 1992; Räisänen 1995). The generalized advective ω-equation exhibits, like its approximate QG counterpart, a similar cancellation of terms, in this case between the differential advection of vertical vorticity $(\boldsymbol{u}_h \cdot \nabla_h \zeta)_z$ and the Laplacian of the advection of density $\nabla_h^2(\boldsymbol{u}_h \cdot \nabla_h \rho)$, since they both include, with opposite signs, the horizontal advection of differential geostrophic vorticity $(\boldsymbol{u}_h \cdot \nabla_h \zeta_z^g)$.

The first generalization of the $\boldsymbol{Q}$-vector ω^q-equation (Davies-Jones 1991) introduced a generalized vector $\boldsymbol{Q}^*$ made up of two contributions, namely a frontogenetical vector $\nabla_h \boldsymbol{u}_h \cdot \nabla_h \rho$ and a vortex-stretching vector $\nabla_h \boldsymbol{u}_h \cdot \boldsymbol{\zeta}_h$, where $\boldsymbol{\zeta}_h = (-v_z, u_z)$ is the relative horizontal pseudovorticity (Hoskins 1975; Davies-Jones 1991). Pseudovorticity ($\boldsymbol{\zeta} = (-v_z, u_z, \zeta)$) may be interpreted as the three-dimensional vorticity of the horizontal (pseudo-plane) flow. More recently Viúdez, Tintoré & Haney (1996*b*) showed that the cancellation in any advective ω-equation is a result of equating the two local rates of change of ζ_z^g obtained from the horizontal momentum and mass conservation equations instead of their material rates of change (or more precisely, their geostrophically advected rates of change). They formulated a $\boldsymbol{Q}$-vector form of the generalized ω-equation (hereafter simply "the ω-equation") and interpreted it as an equation for the material rate of change of the differential ageostrophic vertical vorticity $\zeta_z' \equiv \zeta_z - \zeta_z^g$. The semi-geostrophic version of the $\boldsymbol{Q}$-vector ω-equation (Hoskins 1975; Hoskins & Draghici 1977) extends the QG version by including the ageostrophic advection of the geostrophic horizontal velocity, but leaves out the ageostrophic advection of the ageostrophic horizontal velocity present in the generalized ω-equation. This generalized ω-equation suggests that a

https://doi.org/10.1017/S0022112003004191 Published online by Cambridge University Press

simple generalization of the geostrophic vector $\boldsymbol{Q}^g$ (proportional to $\nabla_h \boldsymbol{u}_h^g \cdot \nabla_h \rho$) is the horizontal frontogenetical vector $\nabla_h \boldsymbol{u}_h \cdot \nabla_h \rho$. Below, we present the first numerical analysis of this ω-equation.

Most of the theoretical, numerical, and experimental work on the ω^q-equation has been for atmospheric applications. Leach (1987) introduced the ω^q-equation in the ocean, and it was first solved in a simplified two-dimensional setting for a density front by Pollard & Regier (1992). More recently, the three-dimensional ω^q-equation (or the semi-geostrophic ω-equation) was solved using high-quality density data for a number of different oceanic fronts and gyres (Viúdez, Tintoré & Haney 1996*c*; Rudnik 1996; Allen & Smeed 1996). Further oceanic applications of the ω^q-equation have involved data assimilation (Viúdez, Haney & Tintoré 1996*a*; Shearman, Barth & Allen 2000; Haney & Hale 2001; Naveira Garabato *et al.* 2001), numerical comparisons (Pinot, Tintoré & Wang 1996), intermediate models using experimental data (Shearman *et al.* 2000), and a study of the errors in w^q due to experimental sampling (Allen *et al.* 2001). The present study carries out the numerical analysis of the full nonlinear ω-equation using simulated data from a baroclinic gyre in the ocean.

Section 2 describes the theoretical basis of the numerical approach. The basic equations are the three-dimensional non-hydrostatic balance of momentum, mass conservation and the isochoric (volume-preserving) condition. The density perturbation is described in terms of the vertical displacement $\mathscr{D}$ of isopycnals. Three potentials $\boldsymbol{\varphi} \equiv (\varphi, \psi, \phi)$ are introduced to describe both the three-dimensional (non-divergent) velocity $\boldsymbol{u} = -\mathrm{curl}\,\boldsymbol{\varphi}$ and the gradient of the scaled isopycnal displacement $D = -\mathrm{div}\,\boldsymbol{\varphi}$, where $D \equiv c^2 \mathscr{D}$ (for details, refer to Dritschel & Viúdez 2003). In this approach, potential vorticity (PV) is explicitly conserved by the advection of PV contours on isopycnal surfaces (using the 'contour advection' algorithm of Dritschel & Ambaum 1997). The theoretical and numerical approach is a new three-dimensional generalization of the two-dimensional explicitly PV-conserving approach used previously to model nonlinear internal gravity waves in the ocean (Viúdez & Dritschel 2002). The final set of equations consists of three prognostic scalar equations: two equations corresponding to the rate of change of the dimensionless ageostrophic horizontal vorticity $\mathscr{A}_h \equiv (\nabla^2\varphi, \nabla^2\psi) = \tilde{\boldsymbol{\omega}}_h - \nabla_h D = \tilde{\boldsymbol{\omega}}_h - \tilde{\boldsymbol{\zeta}}_h^g = \tilde{\boldsymbol{\omega}}_h'$ (where $\tilde{\chi} \equiv \chi/f$ and $\nabla = (\partial_x, \partial_y, \partial_z)$ is the three-dimensional gradient), and the equation for the material conservation of PV, $\dot{\Pi} = 0$. The vertical potential ϕ is obtained, given φ, ϕ, and Π, by inverting the nonlinear definition of PV. This theoretical approach (PV inversion) and the numerical method (advection of PV contours on isopycnals) limit the applicability of our study to static stability processes in the ocean. Statically stable internal gravity waves, with periods shorter than the inertial period and larger than the Brunt–Väisälä period, are also correctly modelled. Smaller scale (sub-mesoscale) phenomena however, like those involving isopycnal overturning and mixing, are therefore excluded.

Section 3 describes the results of a numerical experiment. We study the evolution over 20 inertial periods of a single oceanic baroclinic gyre characterized initially by an ellipsoidal distribution of PV. The simulation domain is triply periodic. A new initialization procedure is used that is based on the progressive growth of the PV field during the first five inertial periods. This procedure largely suppresses the generation of internal-gravity waves, leading to a nearly 'balanced' flow. Since $\tilde{\zeta}_z' = -\nabla_h \cdot \mathscr{A}_h$, the ω-equation may be derived from the divergence of the rate of change of $\mathscr{A}_h$. Every term in the ω-equation is then evaluated from the potentials, and the most relevant terms are visualized using synoptic spatial distributions and grid-point time series.

https://doi.org/10.1017/S0022112003004191 Published online by Cambridge University Press

The analysis carried out here assesses the magnitude of the various terms in the ω-equation in a PV-dominated regime, in which the local change of the materially conserved PV is opposite to its advective rate of change. This is to be distinguished from the internal-gravity-wave-dominated regime, in which the flow is characterized, at least locally, by plane wave solutions and for which there is no local change of PV. The analysis provides a simple explanation for the well-recognized, but still not well-understood, 'over-applicability' of the ω^q-equation. The over-applicability of the ω^q-equation refers to the relatively good agreement of w^q with the total vertical velocity w even for Rossby numbers as large as 0.5. This study suggests that the over-applicability of the ω^q-equation is due to the approximate material conservation of ζ_z'. Contrary to what is assumed when the ω^q-equation is derived from the QG horizontal momentum balance, this equation does not neglect both the local and advective rates of change of ζ_z'. The ω^q-equation does however neglect the material (geostrophically advected) rate of change of ζ_z'. Here it is shown that, for moderately high Rossby numbers in the PV-dominated regime, the local and advective rates of change of ζ_z' are of the same order of magnitude as the largest terms in the ω-equation. However, a large cancellation occurs between these terms, with the result that the material rate of change of ζ_z' is significantly smaller than the local and advective rates of change, and can therefore be neglected in the QG approximation. This quasi-conservation of ζ_z' might be related to the exact material conservation of PV. Finally, some conclusions are given in § 4.

2. Theoretical development

2.1. *Basic equations*

We consider isochoric (volume-preserving) motion in a reference frame rotating with constant angular velocity $f/2$ around the vertical z-axis with respect to an inertial frame. The pressure (plus centripetal potential) is denoted by $\Phi(\boldsymbol{x}, t)$. Vector components here always refer to Cartesian components. The basic equations are the non-hydrostatic balance of linear momentum in a rotating frame, the mass conservation equation and the isochoric condition:

$$\dot{\boldsymbol{u}}_h + f\boldsymbol{k} \times \boldsymbol{u}_h = -\alpha\, \nabla_h \Phi, \tag{2.1a}$$

$$\dot{w} = -\alpha\,(\Phi_z + g\rho), \tag{2.1b}$$

$$\dot{\rho} + \rho\, \nabla \cdot \boldsymbol{u} = 0, \tag{2.1c}$$

$$\nabla \cdot \boldsymbol{u} = 0, \tag{2.1d}$$

where $\alpha \equiv \rho^{-1}$ is the specific volume and g the acceleration due to gravity. The initial unknowns are the three-dimensional velocity field (u, v, w), the pressure Φ, and the density ρ. Subscripts (x, y, z, t) denote partial derivatives. The dot $\dot{(\,)} = \mathrm{d}(\,)/\mathrm{dt} = (\,)_t + \boldsymbol{u} \cdot \nabla(\,)$ denotes the material time derivative (in the rotating frame) and the rest of the symbols have their usual meaning.

2.2. *Mass conservation*

The density anomaly ρ' is defined as $\rho'(\boldsymbol{x}, t) \equiv \rho(\boldsymbol{x}, t) - \varrho_z\, z - \rho_0$, where ρ_0 and ϱ_z are given constants. It is convenient to express ρ in terms of the field d defined by

$$d \equiv (\rho - \rho_0)/\varrho_z. \tag{2.2}$$

The value $d(\boldsymbol{x}, t)$ represents the depth, or vertical location, that an isopycnal located at $\boldsymbol{x}$ at time t has in the reference density configuration defined by $\rho_0 + \varrho_z z$. Thus,

https://doi.org/10.1017/S0022112003004191 Published online by Cambridge University Press

the density field is expressed in terms of distances. The displacement $\mathscr{D}$ of isopycnals with respect to the reference density configuration is

$$\mathscr{D}(\boldsymbol{x}, t) \equiv z - d(\boldsymbol{x}, t). \tag{2.3}$$

Thus, $\mathscr{D}(\boldsymbol{x}, t)$ is the vertical displacement of the isopycnal currently located at $(\boldsymbol{x}, t)$ with respect to its reference position. The incompressibility condition $\dot{\rho} = \dot{d} = 0$ is expressed in terms of $\mathscr{D}$ as

$$\dot{\mathscr{D}} = w. \tag{2.4}$$

In order to define geostrophic quantities, it is also convenient to define a scaled isopycnal vertical displacement

$$D \equiv c^2 \mathscr{D}, \tag{2.5}$$

which is related to ρ by $f^2 D(\boldsymbol{x}, t) - N^2 z = g\,[\rho(\boldsymbol{x}, t)/\rho_0 - 1]$, where $N^2 \equiv -\alpha_0\, g \varrho_z$ is the square of the background Brunt–Väisälä frequency (constant), and $\alpha_0 \equiv \rho_0^{-1}$ is a constant specific volume.

2.3. *Geostrophic quantities*

For any quantity χ let $\tilde{\chi} \equiv \chi/f$. We define the geostrophic velocity shear through the 'thermal wind' expression

$$\tilde{\boldsymbol{u}}_z^g \equiv -\boldsymbol{k} \times \nabla_h D = (D_y, -D_x). \tag{2.6}$$

The relative pseudovorticity is defined in Cartesian components as $\boldsymbol{\zeta} \equiv (-v_z, u_z, \zeta)$, which is the curl of the horizontal velocity. The horizontal gradient of D may be interpreted as the dimensionless horizontal geostrophic pseudovorticity

$$\tilde{\boldsymbol{\zeta}}_h^g = \left(-\tilde{v}_z^g, \tilde{u}_z^g\right) = \nabla_h D. \tag{2.7}$$

Since $\boldsymbol{\zeta}$ is solenoidal ($\nabla \cdot \boldsymbol{\zeta} = 0$) the horizontal divergence of $\tilde{\boldsymbol{\zeta}}_h^g$ is proportional to the differential geostrophic vertical vorticity:

$$-\nabla_h \cdot \tilde{\boldsymbol{\zeta}}_h^g = \left(\tilde{v}_x^g - \tilde{u}_y^g\right)_z = \tilde{\zeta}_z^g = -\nabla_h^2 D. \tag{2.8}$$

Using $\dot{D} = c^2 w$ (2.4), it follows that the rate of change of ∇D may be written

$$\overline{\dot{\nabla D}} = c^2 \nabla w - \nabla \boldsymbol{u} \cdot \nabla D. \tag{2.9}$$

The horizontal component of the above equation expresses the rate of change of $\tilde{\zeta}_h^g$. It is used below to obtain the rate of change of the horizontal ageostrophic vorticity $\mathscr{A}_h = \tilde{\boldsymbol{\omega}}_h - \nabla_h D$.

2.4. *The vorticity equation*

The Cartesian components of the absolute vorticity are $\boldsymbol{\omega}^a \equiv \nabla \times \boldsymbol{u} + f\boldsymbol{k} = (\xi, \eta, \zeta + f)$. The vorticity equation consistent with (2.1) is $\dot{\boldsymbol{\omega}} = \boldsymbol{\omega}^a \cdot \nabla \boldsymbol{u} + \alpha^2 \nabla\rho \times \nabla\Phi$. In the Boussinesq approximation the baroclinic term is $\alpha^2 \nabla\rho \times \nabla\Phi \simeq g\alpha_0^2(-\rho_y, \rho_x, 0) = f^2 \boldsymbol{k} \times \nabla_h D$. Thus, the rate of change of $\tilde{\boldsymbol{\omega}}$ may be written as

$$\dot{\tilde{\boldsymbol{\omega}}} = \tilde{\boldsymbol{\omega}} \cdot \nabla \boldsymbol{u} + \boldsymbol{u}_z + f\boldsymbol{k} \times \nabla_h D, \tag{2.10}$$

and is used below to express the rate of change of $\mathscr{A}_h$.

2.5. *The horizontal ageostrophic vorticity potentials*

We introduce a three-dimensional vector potential $\boldsymbol{\varphi}$ and its Laplacian $\mathscr{A}$ by the definitions

$$\mathscr{A} = (\mathscr{A}, \mathscr{B}, \mathscr{C}) \equiv \nabla^2 \boldsymbol{\varphi} = (\nabla^2\varphi, \nabla^2\psi, \nabla^2\phi) \equiv \tilde{\boldsymbol{\omega}} - \nabla D. \tag{2.11}$$

https://doi.org/10.1017/S0022112003004191 Published online by Cambridge University Press

Taking the divergence of (2.11), and using the identity $\nabla^2\boldsymbol{\varphi} = \nabla(\nabla\cdot\boldsymbol{\varphi}) - \nabla\times\nabla\times\boldsymbol{\varphi}$, we obtain

$$D = -\nabla\cdot\boldsymbol{\varphi}, \quad \tilde{\boldsymbol{u}} = -\nabla\times\boldsymbol{\varphi}, \tag{2.12a, b}$$

showing that D is the 'source' of $-\boldsymbol{\varphi}$, and $-\boldsymbol{\varphi}$ is the velocity potential of $\tilde{\boldsymbol{u}}$. Thus, D is the source of the velocity potential of $\tilde{\boldsymbol{u}}$. Because $\tilde{\boldsymbol{\zeta}}^g_h = \nabla_h D$ by (2.7), the horizontal vector $\mathscr{A}_h = (\mathscr{A}, \mathscr{B})$ may be interpreted as the dimensionless horizontal ageostrophic vorticity

$$\mathscr{A}_h = \tilde{\boldsymbol{\omega}}_h - \tilde{\boldsymbol{\zeta}}^g_h \equiv \tilde{\boldsymbol{\omega}}'_h. \tag{2.13}$$

$\mathscr{A}_h$ is related to the dimensionless horizontal ageostrophic pseudovorticity $\tilde{\boldsymbol{\zeta}}'_h$ (also called the thermal-wind imbalance vector) by $\tilde{\boldsymbol{\omega}}'_h = \tilde{\boldsymbol{\zeta}}'_h - \boldsymbol{k}\times\nabla_h\tilde{w}$. The horizontal divergence and vertical component of the curl of $\mathscr{A}_h$ have the following meanings:

$$\nabla_h\cdot\mathscr{A}_h = -\tilde{\zeta}'_z, \quad \boldsymbol{k}\cdot\nabla\times\mathscr{A}_h = -\nabla^2\tilde{w}, \tag{2.14}$$

where, remarkably, neither $\tilde{\zeta}'_z$ nor $\nabla^2\tilde{w}$ depend on the vertical potential ϕ.

2.6. *The horizontal ageostrophic vorticity equation*

From the rates of change of ∇D (2.9) and $\tilde{\boldsymbol{\omega}}$ (2.10), and using the kinematic relation $\boldsymbol{u}_z = \nabla w - \boldsymbol{k}\times\boldsymbol{\omega}_h$ to express $\boldsymbol{u}_z - c^2\nabla w + f\boldsymbol{k}\times\nabla_h D = (1-c^2)\nabla w - f\boldsymbol{k}\times(\tilde{\boldsymbol{\omega}}_h - \nabla_h D)$, we may finally write the rate of change of $\mathscr{A}$ as

$$\dot{\mathscr{A}} = -f\boldsymbol{k}\times\mathscr{A}_h + (1-c^2)\nabla w + \tilde{\boldsymbol{\omega}}\cdot\nabla\boldsymbol{u} + \nabla\boldsymbol{u}\cdot\nabla D. \tag{2.15}$$

The horizontal component of (2.15) is similar to the equation for the rate of change of the horizontal ageostrophic pseudovorticity $\boldsymbol{\zeta}'_h$ (equation (3.15) in Davies-Jones 1991) except that (2.15) involves the rate of change of the complete horizontal ageostrophic vorticity $\tilde{\boldsymbol{\omega}}'_h$. These horizontal components (the components of $\dot{\mathscr{A}}_h$) are the two scalar prognostic equations integrated in the numerical model. Instead of the vertical component of (2.15), the explicit conservation of PV is used as the third prognostic equation. The horizontal potentials $\boldsymbol{\varphi}_h = (\varphi, \psi)$ are obtained from the inversion $\boldsymbol{\varphi}_h = \nabla^{-2}\mathscr{A}_h$, while the vertical potential ϕ is obtained from the inversion of the definition of PV.

In practice, the horizontal ageostrophic vorticity $\mathscr{A}_h$ is numerically integrated in a triply periodic domain using an explicit leap-frog time-stepping method. Spatial fields are computed using the 'pseudospectral' method, wherein derivatives are computed in spectral space, while nonlinear products are computed on the physical grid, and fast Fourier transforms are used to go from one representation to the other. The numerical parameters are given below.

2.7. *PV inversion and a three-dimensional Monge–Ampère equation*

The dimensionless PV density is defined as

$$\Pi \equiv \tilde{\boldsymbol{\omega}}^a\cdot\nabla d = (\tilde{\boldsymbol{\omega}} + \boldsymbol{k})\cdot(\boldsymbol{k} - \epsilon^2\nabla D) = 1 + \tilde{\zeta} - \epsilon^2 D_z - \epsilon^2\tilde{\boldsymbol{\omega}}\cdot\nabla D.$$

Since $\tilde{\zeta} = \nabla_h^2\phi - \nabla_h\cdot\boldsymbol{\varphi}_{hz}$, and replacing $\tilde{\boldsymbol{\omega}} = \mathscr{A} + \nabla D$, the dimensionless PV anomaly $\varpi \equiv \Pi - 1$ may be written in terms of $\boldsymbol{\varphi}$ as

$$\varpi = \mathscr{L}^q\{\phi\} - (1-\epsilon^2)\nabla_h\cdot\boldsymbol{\varphi}_{hz} + \epsilon^2[\nabla^2\boldsymbol{\varphi} - \nabla(\nabla\cdot\boldsymbol{\varphi})]\cdot\nabla(\nabla\cdot\boldsymbol{\varphi}), \tag{2.16}$$

where the linear operator $\mathscr{L}^q \equiv \epsilon^2 L^q = \nabla_h^2 + \epsilon^2\partial_{zz}$ is the QG Laplacian operator. Since the material conservation of PV,

$$\dot{\varpi} = 0, \tag{2.17}$$

https://doi.org/10.1017/S0022112003004191 Published online by Cambridge University Press

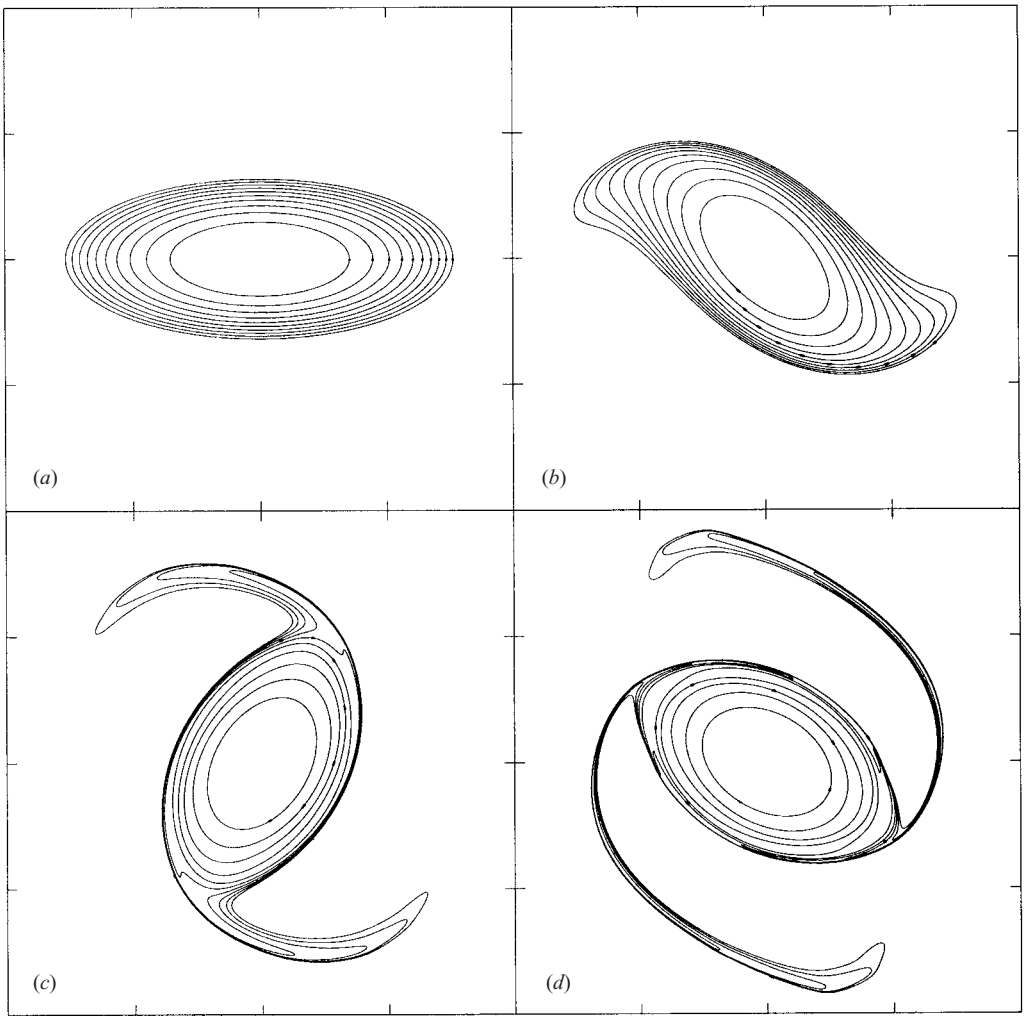


FIGURE 1. Horizontal location of PV contours at $z = 0$ ($i_\rho = 64$) and (*a*) at $t = 0$, (*b*) $t = 5$, (*c*) $t = 10$, and (*d*) $t = 15$ inertial periods. The dots in the contours indicate fluid particles. Domain extent is $10^2([-\pi, \pi] \times [-\pi, \pi])$.

is made explicit in our approach by the advection of PV contours on isopycnal surfaces (Dritschel & Ambaum 1997), equation (2.17) replaces the equation for $\dot{\mathscr{C}}$ in (2.15), and the inversion of (2.16) for ϕ replaces the inversion relation $\phi = \nabla^{-2}\mathscr{C}$. Inversion of (2.16) for the potential ϕ (given φ, ψ, and ϖ) involves a nonlinear (double) Monge–Ampère equation,

$$I_e\left(\phi_{zz}\nabla_h^2\phi - \phi_{xz}^2 - \phi_{yz}^2\right) + I_a\nabla_h^2\phi + 2I_b\phi_{xz} + 2I_b'\phi_{yz} + I_c\phi_{zz} + I_d = 0, \tag{2.18}$$

with coefficients

$$I_a = 1 + \epsilon^2\Theta_z, \quad I_c = \epsilon^2(1 - \Theta_z), \quad I_e = \epsilon^2, \tag{2.19a,b,c}$$

$$I_b = \epsilon^2\left(\tfrac{1}{2}\nabla^2\varphi - \Theta_x\right), \quad I_b' = \epsilon^2\left(\tfrac{1}{2}\nabla^2\psi - \Theta_y\right), \tag{2.19d,e}$$

$$I_d = \epsilon^2[\Theta_x\nabla^2\varphi + \Theta_y\nabla^2\psi - (\nabla\Theta)^2] - (1 - \epsilon^2)\Theta_z - \varpi, \tag{2.19f}$$

and where $\Theta \equiv \nabla_h \cdot \boldsymbol{\varphi}_h$.

https://doi.org/10.1017/S0022112003004191 Published online by Cambridge University Press

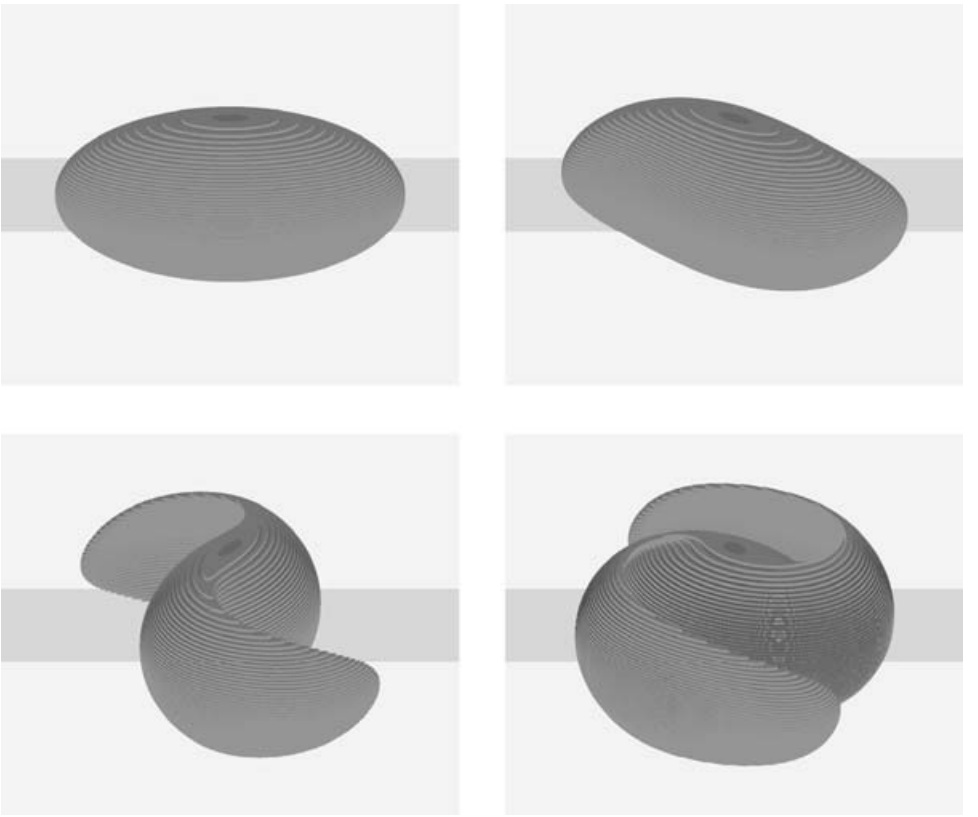


FIGURE 2. Three-dimensional view of the PV contours (*a*) at $t = 0$, (*b*) $t = 5$, (*c*) $t = 10$ and (*d*) $t = 15$ inertial periods.

The numerical procedure used to solve this nonlinear equation is based on iteration. We collect the linear, constant-coefficient terms of ϕ on the left-hand side, and consider all remaining terms (computed using a previous guess for ϕ) as a source on the right-hand side. The result is an equation of the form

$$\mathscr{L}^q\{\phi\} = S\{\boldsymbol{\varphi}\}, \tag{2.20}$$

where S is the 'source'. Given S, this equation is trivially inverted in spectral space to find a new approximation to ϕ. If this approximation differs by less than a prescribed tolerance (here 10^{-7}) from the previous approximation, the solution is accepted. Otherwise, S is recomputed using the new ϕ (all other potentials remain unchanged), and the procedure is repeated. This procedure normally converges in a few iterations, except when Π is close to zero or is very large.

2.8. *The generalized ω-equation*

The generalized ω-equation can be obtained from the horizontal divergence of (2.15). Since $\nabla_h \cdot \mathscr{A}_h = -\tilde{\zeta}'_z$ (2.14) the ω-equation may be interpreted as the equation for the rate of change of $\tilde{\zeta}'_z$. Defining the vector $\boldsymbol{Q}_h \equiv \nabla_h \boldsymbol{u}_h \cdot \nabla_h D$, the ω-equation (Viúdez *et al.* 1996*b*) can be written as

$$\mathrm{d}\tilde{\zeta}'_z/\mathrm{d}t = -\nabla_h \cdot [2\boldsymbol{Q}_h + (D_z - c^2)\nabla_h w] + (\tilde{\zeta} + 1)w_{zz} + \tilde{\boldsymbol{\zeta}}'_{hz} \cdot \nabla_h w - \tilde{\boldsymbol{\zeta}}'_h \cdot \nabla_h^2 \boldsymbol{u}_h\,. \tag{2.21}$$

https://doi.org/10.1017/S0022112003004191 Published online by Cambridge University Press

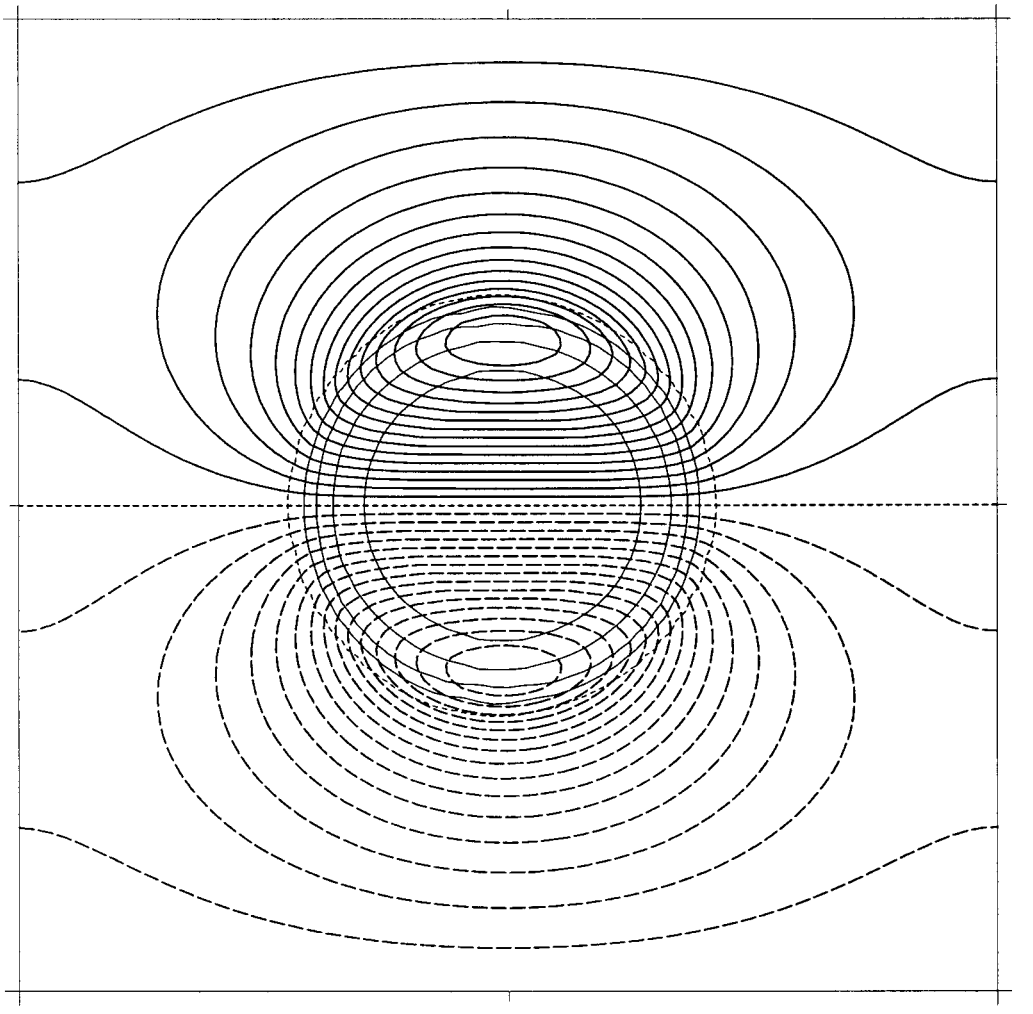


FIGURE 3. Vertical distribution at $y = 0$ (grid point $i_Y = 32$) and at $t = 11$ i.p. of $\mathscr{D}$ (thick lines, contour interval $\Delta = 1 \times 10^{-2}$, extreme contour values $\pm 16 \times 10^{-2}$) and gridded PV (thin lines, $\Delta = 0.1$, minimum contour value -0.4). Domain extent is $(10^2[-\pi, \pi]) \times [-\pi, \pi]$. In this and subsequent similar figures, solid lines are for positive values, dashed lines negative, and the short-dashed line is the zero contour.

Under the QG approximation, the horizontal velocity is replaced by its geostrophic approximation ($\boldsymbol{u}_h \to \boldsymbol{u}_h^g$), and assuming that for small Rossby numbers the flow is both inertially very stable ($|\tilde{\zeta}| \ll 1$) and statically very stable ($|D_z| \ll c^2$), we may derive the $\boldsymbol{Q}$-vector ω^q-equation

$$L^q\{w^q\} = 2\nabla_h \cdot \boldsymbol{Q}_h^g\,, \tag{2.22}$$

where $\boldsymbol{Q}_h^g \equiv \nabla_h \boldsymbol{u}_h^g \cdot \nabla_h D$ is the horizontal geostrophic $\boldsymbol{Q}$-vector. For diagnostic purposes, in the numerical code this linear equation is directly solved for w^q by inverting the operator L^q in spectral space.

https://doi.org/10.1017/S0022112003004191 Published online by Cambridge University Press

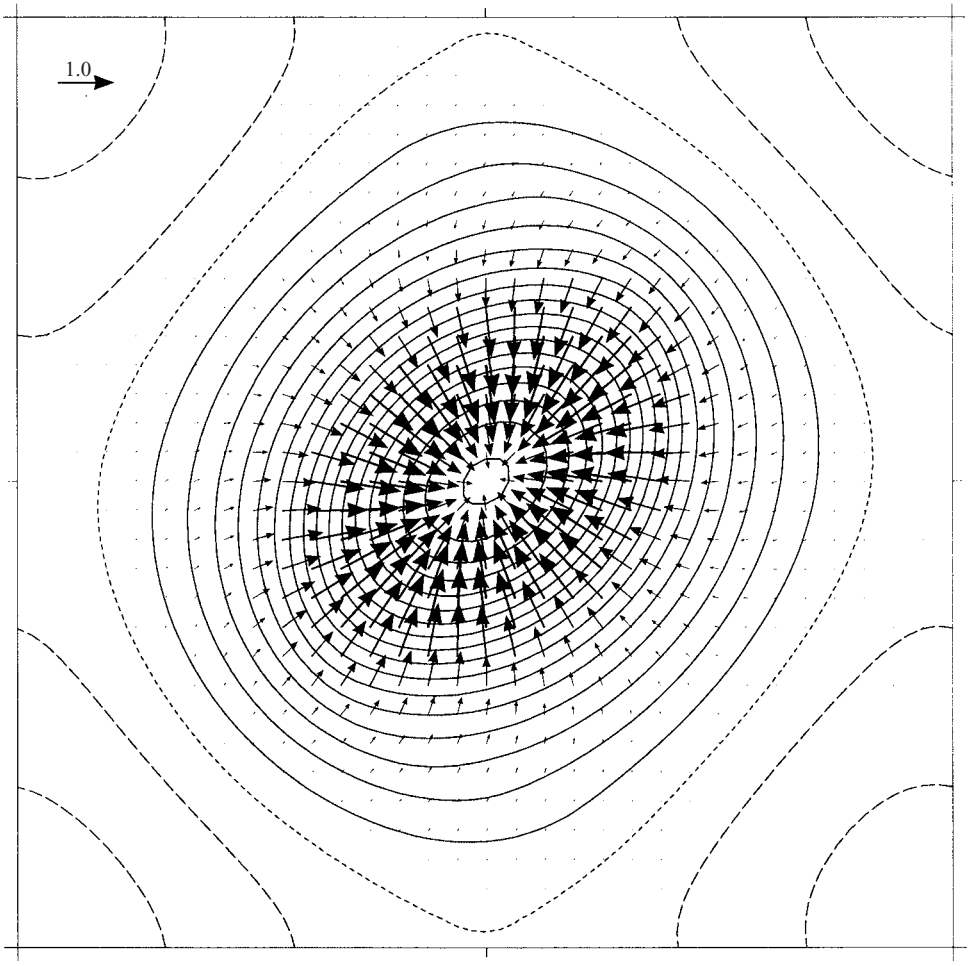


FIGURE 4. Horizontal distribution at $z = -0.74$ ($i_Z = 50$) and at $t = 11$ i.p. of $\boldsymbol{\varphi}_h$ and ϕ (contour interval $\Delta = 1 \times 10^{-2}$).

3. Numerical results

This section describes the evolution over 20 inertial periods of a single baroclinic gyre initially defined by a three-dimensional ellipsoidal distribution of PV.

3.1. *Numerical parameters and initial set-up of the gyre*

We consider a domain having $(n_X, n_Y, n_Z) = (64, 64, 128)$ grid points, a vertical extent $L_Z = 2\pi$ (in arbitrary space units) and horizontal extents L_X and L_Y prescribed by the ratios $L_X/L_Z = L_Y/L_Z = 100$. This ratio is equal to the ratio of the mean Brunt–Väisälä to Coriolis frequency $c \equiv N/f = 100$, where $N = 2\pi$ (in arbitrary time units). Thus the time interval of one (mean) buoyancy period (b.p.) is $\Delta t = 1$. One inertial period (i.p.) equals 100 b.p. The time step is set to $\delta t = 0.1$ (a tenth of a buoyancy period). The number of isopycnal surfaces n_l is set equal to the number of grid points in the vertical direction, $n_l = n_Z = 128$.

For simplicity the initial PV anomaly distribution is taken to be an ellipsoidal vortex, within which the PV varies only across nested ellipsoidal surfaces. The PV anomaly, ϖ, constant on ellipsoidal surfaces, varies linearly with the ellipsoidal volume, with

https://doi.org/10.1017/S0022112003004191 Published online by Cambridge University Press

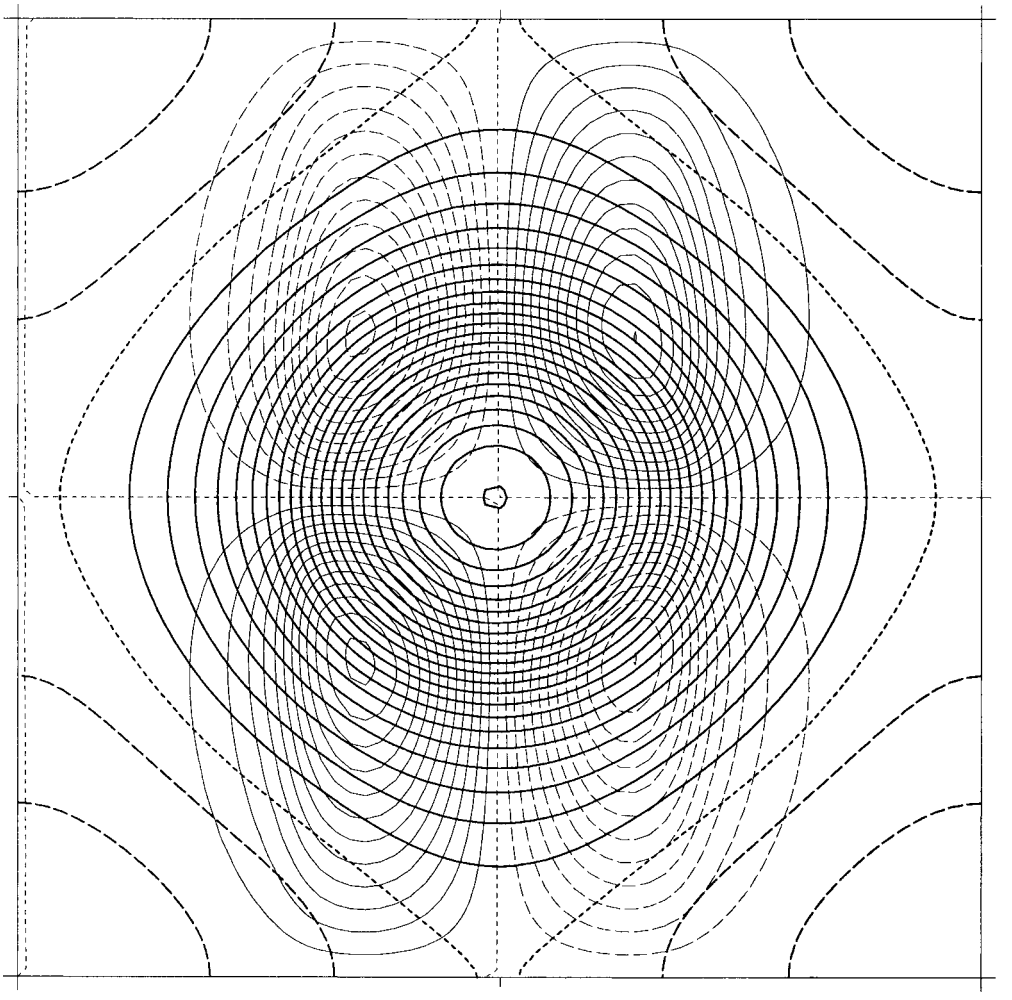


FIGURE 5. Vertical distribution (as in figure 3) of φ (thin lines, $\Delta = 1 \times 10^2$) and ϕ (thick lines, $\Delta = 0.1$).

$\varpi = 0$ on the outermost surface, and $\varpi = \varpi_i$ at the core. Since the domain integral of ϖ must vanish in the periodic domain used, there is a small background PV anomaly ϖ_b everywhere outside the vortex. This PV distribution is discretized by placing a number of PV contours within each isopycnal surface crossing through the vortex. The middle isopycnal surface ($i_\rho = 64$) has the maximum number of contours, $n_c = 10$. Between each contour, ϖ is uniform, and across each contour ϖ jumps by a fixed increment of $\Delta\varpi \equiv (\varpi_i - \varpi_b)/n_c$, except for the outermost contour where ϖ jumps by $\Delta\varpi/2$ (see Dritschel 1998).

The initial PV contours (figures 1 and 2) are ellipses with a ratio of major (a_M) to minor (a_m) axes lengths $r_e = a_M/a_m = 2.4$. In the middle surface $i_\rho = 64$ the largest ellipse has $a_M = 4.8c$ and $a_m = 2.0c$. On the other isopycnals, we keep the same horizontal aspect ratio but reduce the axis lengths to fit within a three-dimensional ellipsoid of vertical axis length equal to a_m in the scaled (x, z)-plane (figures 2 and 3).

https://doi.org/10.1017/S0022112003004191 Published online by Cambridge University Press

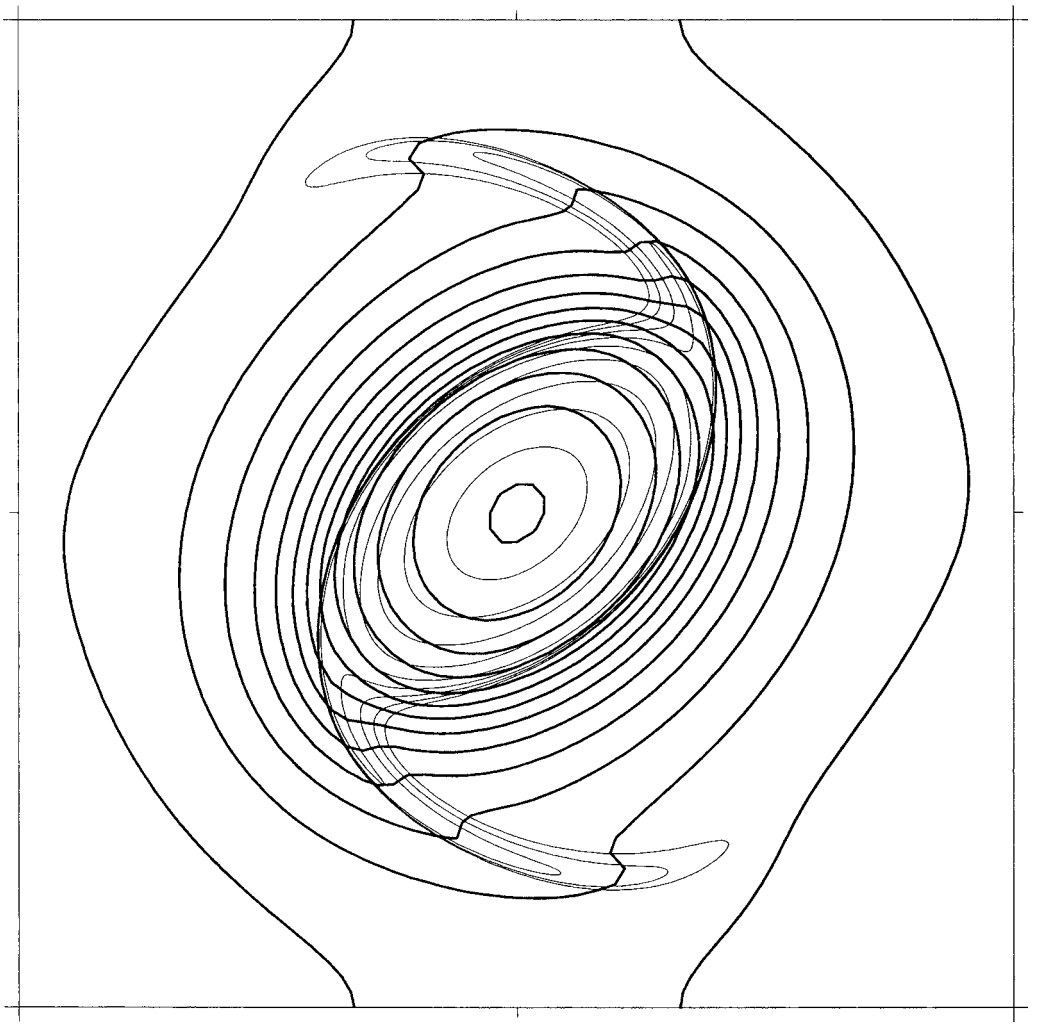


FIGURE 6. Horizontal distribution (as in figure 4) of $\mathscr{D}$ (thick lines, $\Delta = 1 \times 10^{-2}$, with minimum contour -13×10^{-2}) and PV contours on $i_\rho = 52$ (thin lines).

The PV anomaly at the centre of the vortex is set to $\Delta\varpi = -0.5$ at the end of the initialization procedure described below. This corresponds to an anticyclonic gyre when the motion is in near geostrophic balance.

3.2. *Interpolation procedure*

The PV evolution is carried out by explicitly tracking material contours on isopycnal surfaces. However, much of the numerical code is grid based, so it is necessary to convert these PV contours to a three-dimensional gridded field (e.g. for solving the Monge–Ampère equation). The procedure adopted follows the 'contour-to-grid' conversion procedure introduced by Dritschel & Ambaum (1997). On each isopycnal surface, horizontal grid line crossings are sought for each contour, and this information enables one to build the gridded PV field – on this surface. Here, unlike in Dritschel & Ambaum (1997), we furthermore interpolate the PV from isopycnal surfaces to

https://doi.org/10.1017/S0022112003004191 Published online by Cambridge University Press

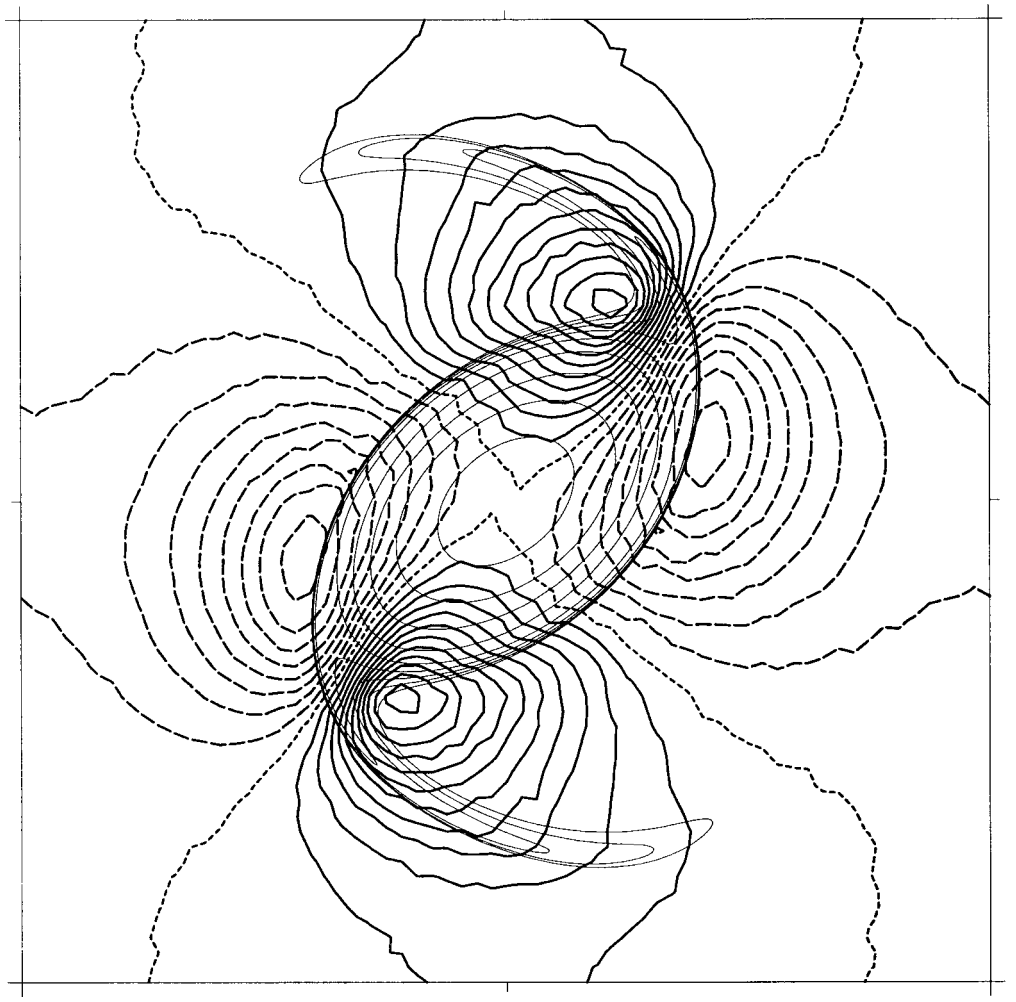


FIGURE 7. Horizontal distribution (as in figure 6) of w (thick lines, $\Delta = 1 \times 10^{-5}$) and PV contours on $i_\rho = 52$ (thin lines).

equally spaced vertical grid points. Linear interpolation is used between adjacent isopycnals, for a fixed horizontal grid point.

3.3. *Initialization procedure*

Since a gyre is never in exact geostrophic balance (in part because of its centripetal acceleration), an initialization procedure must be carried out to avoid the initial generation of internal gravity waves by spontaneous adjustment. Otherwise, fields of interest like the vertical velocity would be swamped by imbalanced motions, rendering any diagnostic of balanced motion useless. This is particularly true of the vertical velocity, whose balanced component is typically 10^4 times smaller than horizontal velocities. The initialization procedure must be good enough to suppress all internal gravity waves having vertical velocity amplitudes larger than or comparable to the typical amplitude of the mesoscale vertical velocity.

https://doi.org/10.1017/S0022112003004191 Published online by Cambridge University Press

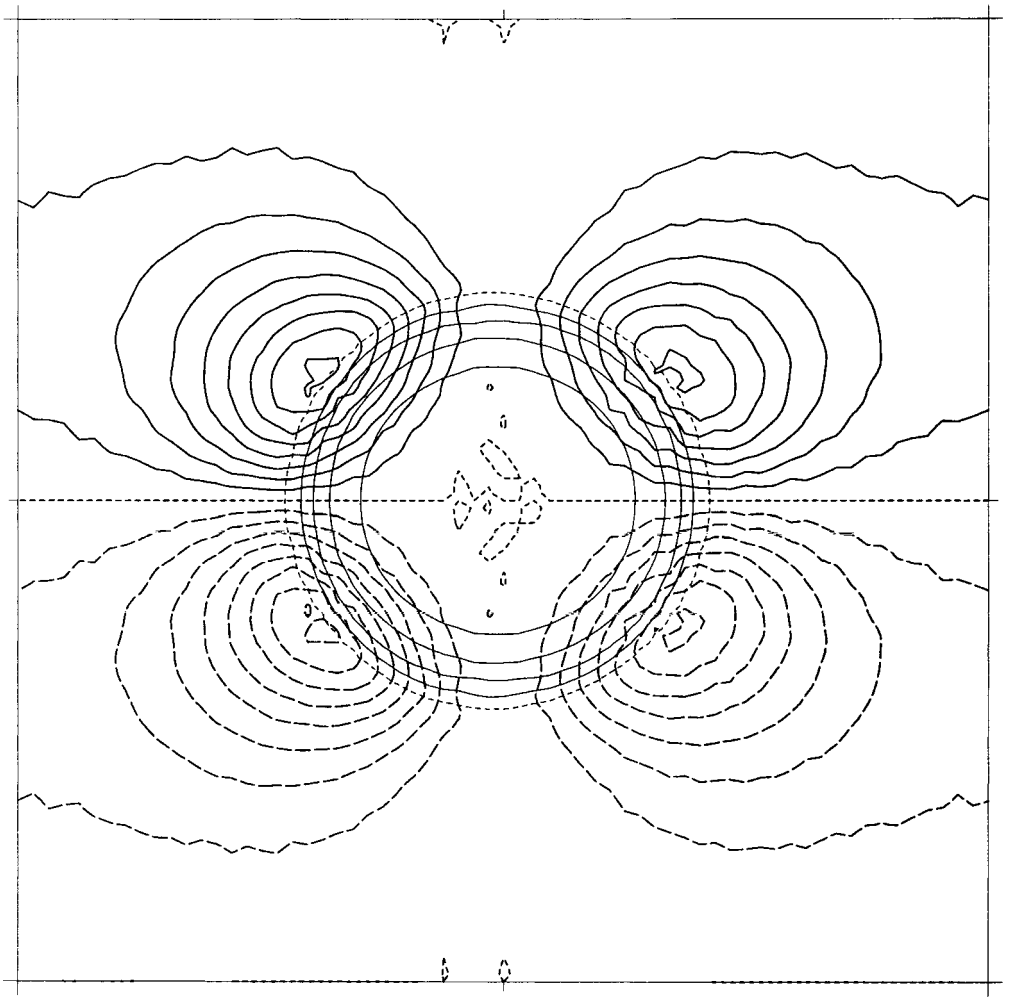


FIGURE 8. Vertical distribution (as in figure 3) of w (thick lines, $\Delta = 1 \times 10^{-5}$) and gridded PV (thin lines, $\Delta = 0.1$, minimum contour value -0.4).

The initialization procedure used here is based on the slow, progressive growth of the PV field during an initial time interval from $t = 0$ to $t = t_i$. In practice, we have found that $t_i = 500$ (5 i.p.) is sufficient to avoid significant excitation of internal gravity waves, leading to a nearly balanced flow. The implementation of this procedure in our explicitly PV-conserving numerical method is remarkably straightforward. During the initialization period, the gridded PV field $\varpi(\boldsymbol{x}, t)$ (found at every time step by the PV interpolation procedure described above) is multiplied by a weight $W(t)$, here given by

$$W(t) \equiv \tfrac{1}{2}(1 - \cos(\pi t / t_i)) \,. \tag{3.1}$$

Note that W is smooth at $t = 0$ and at $t = t_i$ ($W(0) = 0$, $W(t_i) = 1$, $W_t(0) = W_t(t_i) = 0$). This smoothness was found to help minimize the initial generation of internal gravity waves. The weight (3.1) produced better results than a linear ramp.

https://doi.org/10.1017/S0022112003004191 Published online by Cambridge University Press

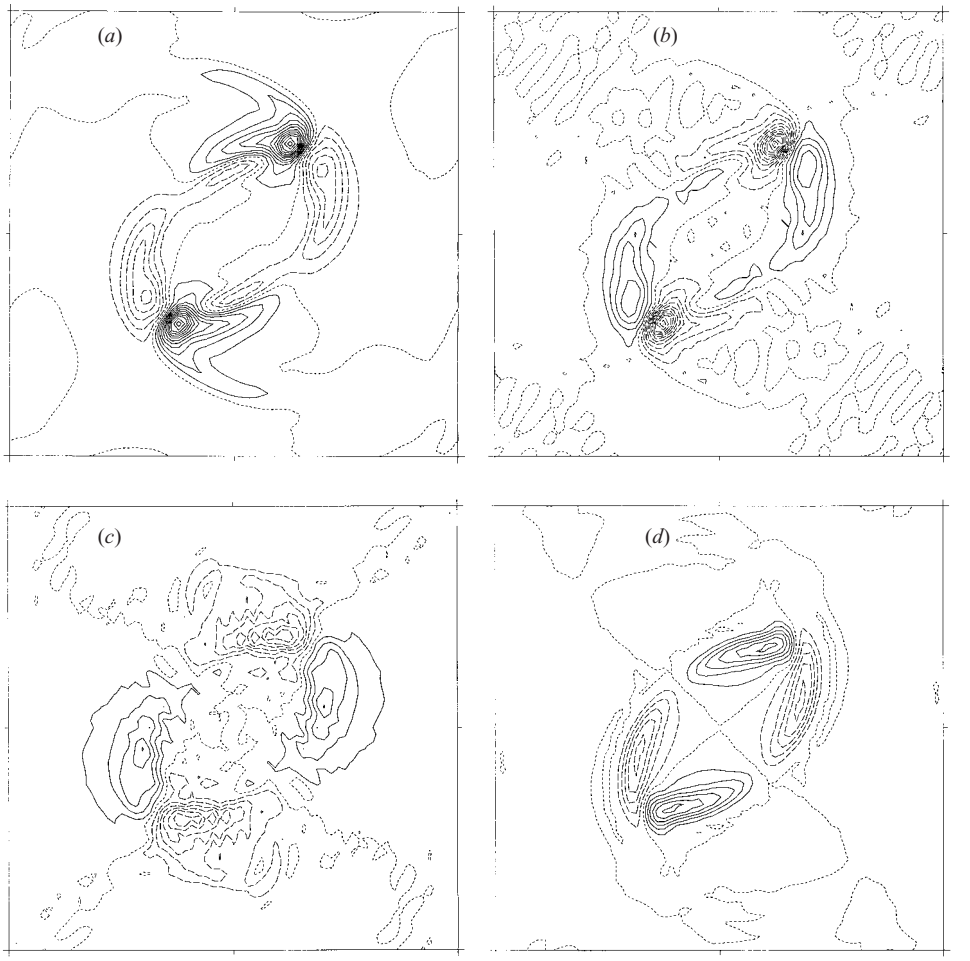


FIGURE 9. Horizontal distribution (as in figure 4) of (*a*) $-2\nabla_h \cdot \boldsymbol{Q}_h$ ($\Delta = 2 \times 10^{-4}$), (*b*) $c^2\nabla_h^2 w$ ($\Delta = 2 \times 10^{-4}$), (*c*) w_{zz} ($\Delta = 1 \times 10^{-4}$), and (*d*) $-\tilde{\boldsymbol{\zeta}}_h' \cdot \nabla_h^2 \boldsymbol{u}_h$, ($\Delta = 1 \times 10^{-4}$).

3.4. *Analysis*

3.4.1. *PV, potentials, and displacement*

The PV evolution (figures 1 and 2) shows that the outer part of the anticyclonic vortex is swept into a large filament encircling the faster-rotating vortex core. The vertical extent and symmetry of the PV vortex at the end of the initialization period ($t = 5$ i.p.) is shown in figure 3. The vortex core becomes more axisymmetric and does not continue shedding PV (compare the inner PV ellipse at $t = 0$ and $t = 15$ i.p.). This filamentation and subsequent stabilization of the gyre takes place in a similar way on every isopycnal surface, as is evident from the three-dimensional PV contour images in figure 2.

In the following analysis we select $t = 11$ i.p. as a representative time in the vortex evolution. At this time the vortex is well beyond the end of the initialization period ($t_i = 5$ i.p.), and moreover its shape (with its major axis lying between the x- and y-axes) is convenient for plotting purposes. The horizontal vector potential $\boldsymbol{\varphi}_h$ at this time (figure 4) is directed toward the centre of the gyre at negative depths. At positive

https://doi.org/10.1017/S0022112003004191 Published online by Cambridge University Press

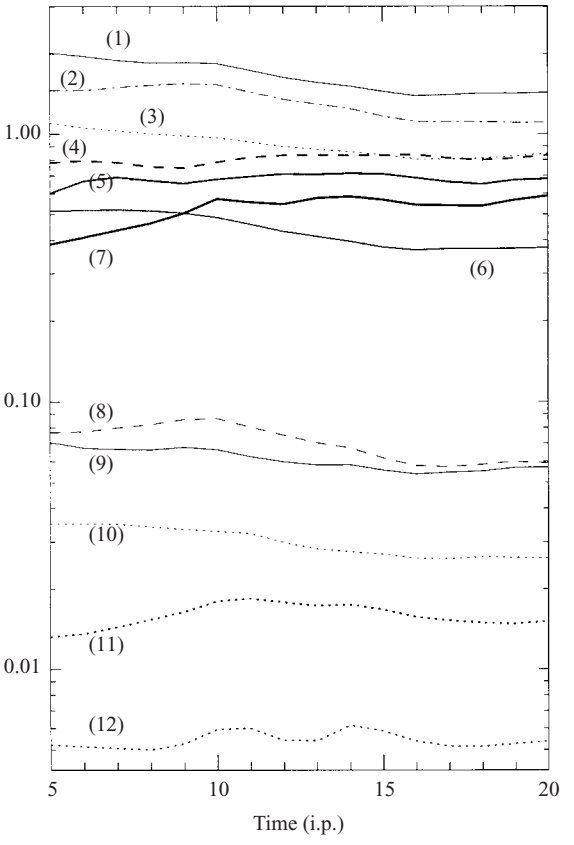


FIGURE 10. Domain-average time series of the absolute value of $-2\nabla_h \cdot \boldsymbol{Q}_h$ (1), $c^2\nabla_h^2 w$ (2), w_{zz} (3), $\tilde{\zeta}'_{zt}$ (4), $\boldsymbol{u}_h \cdot \nabla_h \tilde{\zeta}'_z$ (5), $-\tilde{\boldsymbol{\zeta}}'_h \cdot \nabla_h^2 \boldsymbol{u}_h$ (6), $\tilde{\zeta}'_{zt} + \boldsymbol{u}_h \cdot \nabla_h \tilde{\zeta}'_z$ (7), $-D_z \nabla_h^2 w$ (8), $\tilde{\zeta} w_{zz}$ (9), $-\nabla_h D_z \cdot \nabla_h w$ (10), $w\tilde{\zeta}'_{zz}$ (11), and $\tilde{\boldsymbol{\zeta}}'_{hz} \cdot \nabla_h w$ (12). A logarithmic scale, in units of 10^{-4}, is used for the vertical axis. The average is restricted to those locations having a kinetic energy larger than the domain-average value.

depths the opposite occurs, showing that the horizontal potentials (φ, ψ) each have an octupole distribution with eight extrema (figure 5). The vertical potential ϕ is typically three orders of magnitude larger than φ and ψ and has an almost spherical shape with a maximum value at the core of the gyre (compare figures 4 and 5).

The vertical displacement $\mathscr{D}$ of isopycnals (figures 3 and 6) is greatest where the largest vertical PV gradients occur. Positive displacement (elevated isopycnals) occurs in the lower part of the gyre, while negative displacement (depressed isopycnals) occurs in the upper part. The filamentation of PV appears in $\mathscr{D}$ (figure 6) as frontal anomalies on the otherwise elliptical $\mathscr{D}$ contours.

3.4.2. *Vertical motion from PV conservation*

From the horizontal distributions of PV and $\mathscr{D}$ (figure 6 shows the lower part of the domain), it is possible to infer the sign of the vertical motion. First notice that the contours of $\mathscr{D}$ and PV move anticyclonically with the same phase speed, and that, qualitatively, the $\mathscr{D}$ contours form wider ellipses than the PV contours (the $\mathscr{D}$ and PV contours intersect). Thus, since fluid particles move along PV contours faster than the

https://doi.org/10.1017/S0022112003004191 Published online by Cambridge University Press

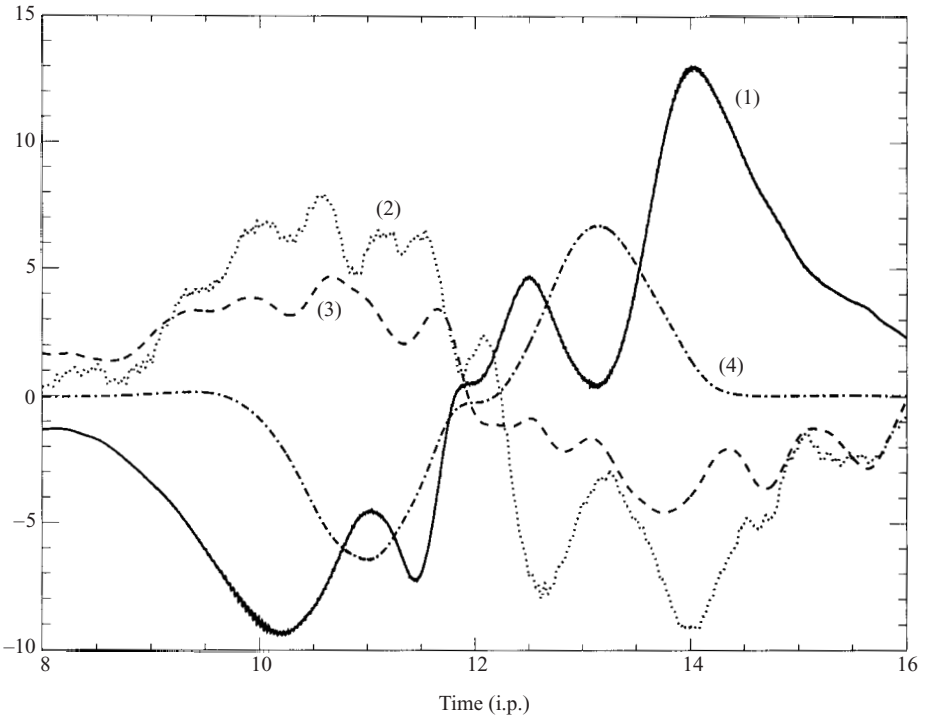


FIGURE 11. Time series at grid point $(i_X, i_Y, i_Z) = (45, 38, 50)$ (i.e. $(x, y, z) \simeq (1.2 \times 10^2, -0.50 \times 10^2, -0.74)$) from $t = 8$ to $t = 16$ i.p. of $-2\nabla_h \cdot \boldsymbol{Q}_h$ (1), $c^2\nabla_h^2 w$ (2), w_{zz} (3), and $-\tilde{\boldsymbol{\zeta}}_h' \cdot \nabla_h^2 \boldsymbol{u}_h$ (4). The vertical axis is in units of 10^{-4}.

phase speed (cf. figure 1), the fluid particles approaching the vertex of the PV ellipse must climb the isopycnal surface (and hence have $w > 0$). Similarly, fluid particles leaving the vertex of the PV ellipse must move down the isopycnal surface (and hence have $w < 0$). In the upper part of the domain (figure 3) the PV contours have the same shape as illustrated here, but the displacement has the opposite sign. This implies that the vertical velocity is exactly reversed in the upper half of the domain, and overall has an octupole structure. As the vortex becomes more axisymmetric, the PV ellipse widens (figure 1) and the difference between the PV and $\mathscr{D}$ ellipses becomes less pronounced. As a result, the vertical velocity decreases in magnitude at later times.

3.4.3. *Vertical velocity*

The vertical velocity w (figures 7 and 8) is consistent with the inferences made above. The field w has an octupole structure with vertical symmetry and symmetry with respect to the central point in the domain. Extreme values of w occur at the edge of the PV ellipsoid. The upward vertical velocity at the rear edge of the clockwise-rotating PV vortex (maximum value: 1.1×10^{-4}) has a magnitude larger than the downward velocity at the leading PV edge (maximum value: 0.9×10^{-4}). These values are four orders of magnitude smaller than the maximum horizontal speeds, which are roughly 1 on the middle isopycnal surface.

https://doi.org/10.1017/S0022112003004191 Published online by Cambridge University Press

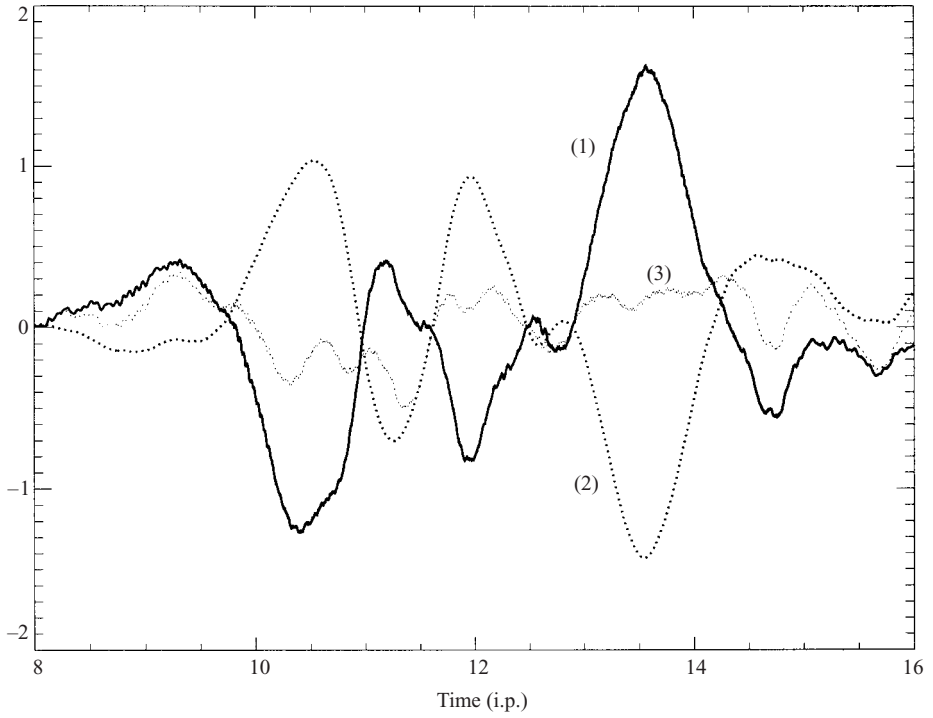


FIGURE 12. As in figure 11 but for $\tilde{\zeta}'_{zt}$ (1), $\boldsymbol{u}_h \cdot \nabla_h \tilde{\zeta}'_z$ (2), and $\tilde{\zeta}'_{zt} + \boldsymbol{u}_h \cdot \nabla_h \tilde{\zeta}'_z$ (3). The vertical axis is in units of 10^{-3}.

3.4.4. *Analysis of the generalized ω-equation*

We now analyse every term in the generalized ω-equation (2.21) and see how these are related to the vertical velocity. Equation (2.21) is decomposed term by term as

$$\tilde{\zeta}'_{zt} + \boldsymbol{u}_h \cdot \nabla_h \tilde{\zeta}'_z + w\tilde{\zeta}'_{zz} = -2\nabla_h \cdot \boldsymbol{Q}_h - \nabla_h D_z \cdot \nabla_h w - D_z \nabla_h^2 w + c^2 \nabla_h^2 w + w_{zz} + \tilde{\zeta} w_{zz} + \tilde{\boldsymbol{\zeta}}'_{hz} \cdot \nabla_h w - \tilde{\boldsymbol{\zeta}}'_h \cdot \nabla_h^2 \boldsymbol{u}_h. \quad (3.2)$$

One of the largest terms in (3.2) is $-2\nabla_h \cdot \boldsymbol{Q}_h$ (see its horizontal distribution in figure 9*a*). This has large magnitude along the edge of the vortex, with extrema on both sides of every vertex. The maxima and minima are clearly related to the maxima and minima of w (compare with figure 7). The filamentary PV anomalies are also clearly observed in figure 9(*a*) though these are of second order in importance. Spatial-average time series (figure 10) show that this term is the largest, in an average sense, over the evolution of the vortex. Time series at one location (figure 11) show however that at certain times other terms in (3.2) may be larger.

The next most important term is $c^2\nabla_h^2 w$, as seen from the spatial-average time series (figure 10). Its horizontal distribution (figure 9*b*) shows that it is largely opposite in sign to $-2\nabla_h \cdot \boldsymbol{Q}_h$ so that a significant cancellation of these two terms occurs (see figure 9*a* and the time series at one location in figure 11). However $c^2\nabla_h^2 w$ also contains second-order contributions from small internal gravity waves generated apparently by the vortex filamentation.

We next group together three different terms of similar magnitude in their spatial averages. The first one is w_{zz}. This term exhibits an octupole structure with

https://doi.org/10.1017/S0022112003004191 Published online by Cambridge University Press

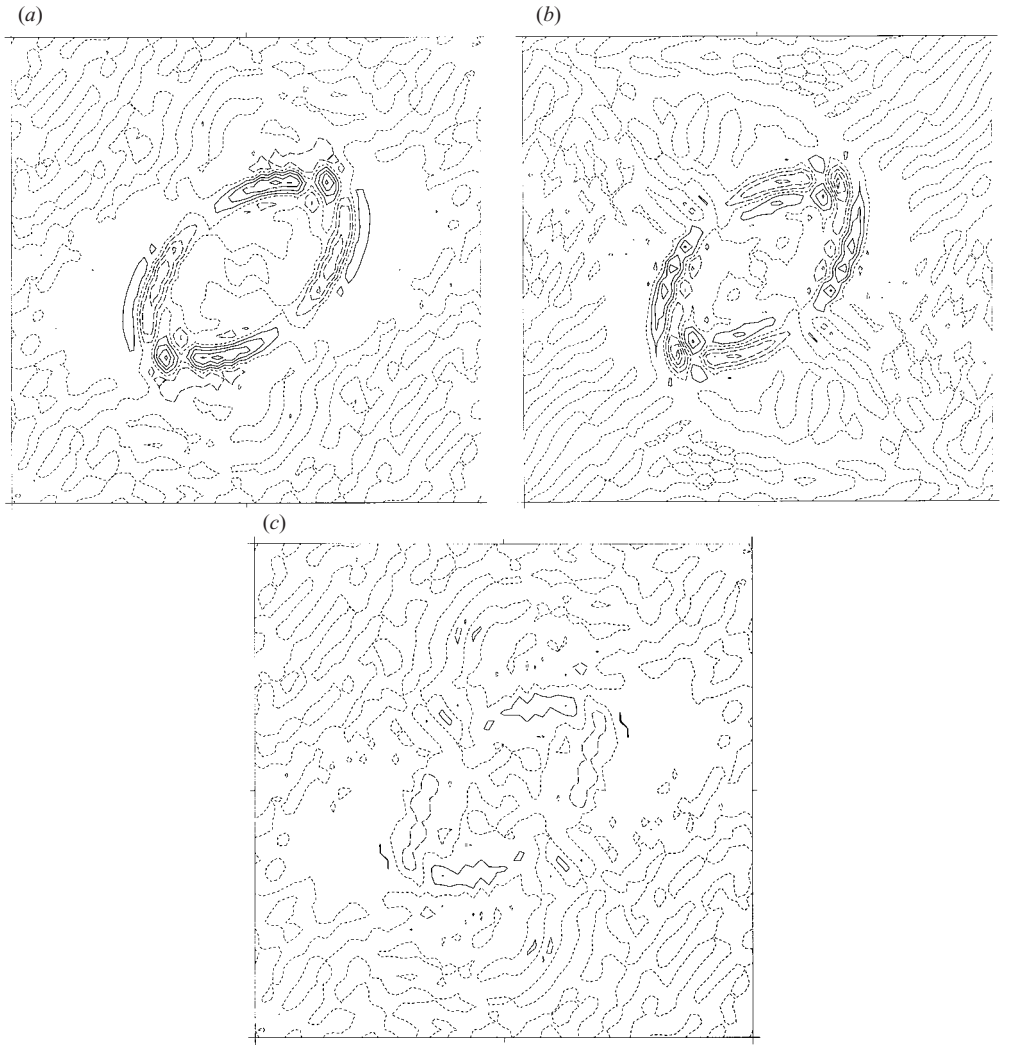


FIGURE 13. Horizontal distribution (as in figure 4) of (*a*) $\tilde{\zeta}'_{zt}$, (*b*) $\boldsymbol{u}_h \cdot \nabla_h \tilde{\zeta}'_z$, and (*c*) $\tilde{\zeta}'_{zt} + \boldsymbol{u}_h \cdot \nabla_h \tilde{\zeta}'_z$. Contour interval $\Delta = 2 \times 10^{-4}$.

second-order internal waves (figure 9*c*) and is broadly similar to $c^2 \nabla_h^2 w$. The times series (figure 11) confirm that the sign of both terms coincides and that w_{zz} has a smaller magnitude in an average sense (figure 11).

The two other terms in this group are the local rate of change of differential ageostrophic vorticity ($\tilde{\zeta}'_{zt}$) and its horizontal advection ($\boldsymbol{u}_h \cdot \nabla_h \tilde{\zeta}'_z$). The spatial distribution and magnitude of these two terms in the context of the ω-equation are among the most important findings in this work and, consequently, we examine these terms in a little more detail. At some locations, these two terms are the largest ones in the ω-equation (figure 12). Their spatial averages are of the same order of magnitude as, though smaller than, the spatial averages of $-2\nabla_h \cdot \boldsymbol{Q}_h$ and $c^2 \nabla_h^2 w$ (figure 10). However, both terms show significant cancellation, implying that $\tilde{\zeta}'_{zt}$ is conserved to first order within the vortex (mesoscale) motion. As a result their joint contribution to the ω-equation is significantly smaller. The local rate of change of $\tilde{\zeta}'_z$

https://doi.org/10.1017/S0022112003004191 Published online by Cambridge University Press

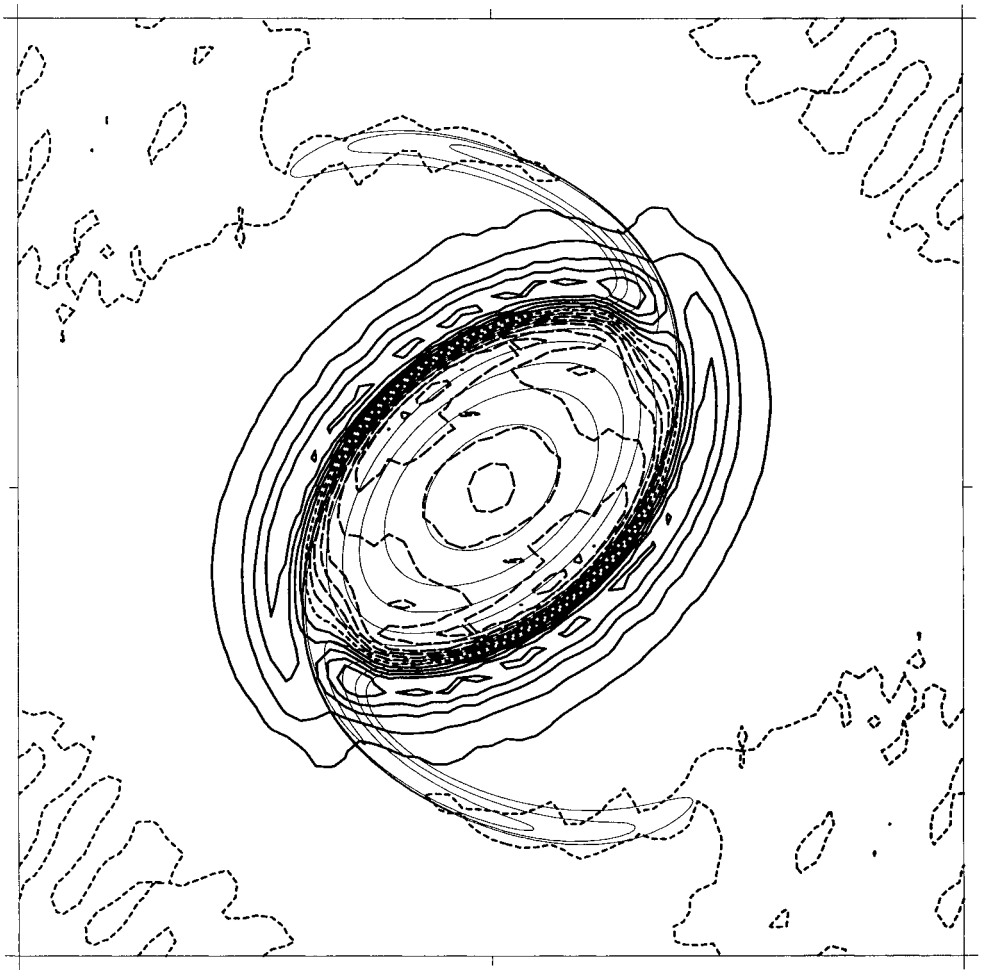


FIGURE 14. As in figure 6 but for $\tilde{\zeta}_z'$ (thick lines, $\Delta = 1 \times 10^{-6}$) and PV contours (thin lines).

and the term w_{zz} are of the same order of magnitude (0.8×10^{-4}) in spatial averages (figure 10), while the average material rate of change of $\tilde{\zeta}_z'$ is smaller than any of the three QG terms and therefore may be consistently neglected.

The approximate cancellation between these terms is also apparent in their horizontal distributions (figure 13). These display alternating bands of positive and negative values along the outer part of vortex, with an almost constant zero value at the core. These distributions can be understood from the horizontal distribution of $\tilde{\zeta}_z'$ (figure 14). The differential ageostrophic vorticity exhibits positive extrema outside the vortex and negative inside. Since $\tilde{\zeta}_z'$ is almost materially advected as the vortex rotates, an observer located at a fixed spatial location would measure an increase and then a decrease of $\tilde{\zeta}_z'$ as the tip (or vertex) of the vortex core passes over, followed by a second increase and decrease of $\tilde{\zeta}_z'$ as the vortex core leaves. The pattern of $\tilde{\zeta}_{zt}'$ in figure 13 can be thus understood from the approximate material advection of $\tilde{\zeta}_z'$.

The magnitude of $-\tilde{\boldsymbol{\zeta}}_h' \cdot \nabla_h^2 \boldsymbol{u}_h$ has a spatially averaged value of 0.4×10^{-4}, but locally may be as important as the largest terms (figure 11). This term (see figure 9*d*) has an octupole structure similar to $-2\nabla_h \cdot \boldsymbol{Q}_h$ (figure 9*a*). Below this term in figure 10 there is

https://doi.org/10.1017/S0022112003004191 Published online by Cambridge University Press

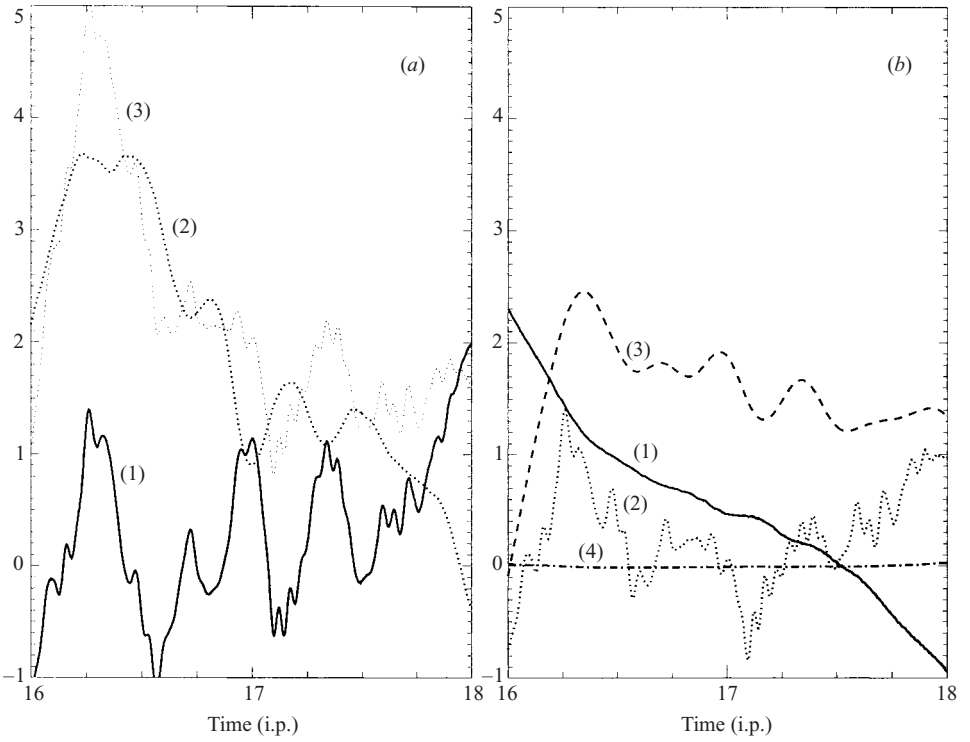


FIGURE 15. (*a*) As in figure 12 but from $t = 16$ to $t = 18$ i.p., $\tilde{\zeta}'_{zt}$ (1), $\boldsymbol{u}_h \cdot \nabla_h \tilde{\zeta}'_z$ (2), and $\tilde{\zeta}'_{zt} + \boldsymbol{u}_h \cdot \nabla_h \tilde{\zeta}'_z$ (3). (*b*) As in figure 11 but from $t = 16$ to $t = 18$ i.p., $-2\nabla_h \cdot \boldsymbol{Q}_h$ (1), $c^2 \nabla_h^2 w$ (2), w_{zz} (3), and $-\tilde{\boldsymbol{\zeta}}'_h \cdot \nabla_h^2 \boldsymbol{u}_h$ (4). The vertical axes are in units of 10^{-4}.

a large gap in magnitude to the remaining terms in (3.2), which are clearly of second and third order (their distributions are not shown here). Thus, for consistency, an improved ω^q-equation should retain this term as a priority over any other remaining term in the ω-equation. Note particularly that the term $\tilde{\zeta} w_{zz}$ is clearly smaller than $-\tilde{\boldsymbol{\zeta}}'_h \cdot \nabla_h^2 \boldsymbol{u}_h$ and of the same order of magnitude as, though also smaller than, the term $-D_z \nabla_h^2 w$.

3.4.5. *Internal wave vertical motion*

The parts of the flow outside the PV-dominated region exhibit a different balance in the ω-equation. The time series at the same grid point shown in figures 11 and 12 but for the next two inertial periods, once the PV vortex has passed this location, shows that the maxima of $\tilde{\zeta}'_{zt}$ and $\boldsymbol{u}_h \cdot \nabla_h \tilde{\zeta}'_z$ have decreased by one order of magnitude (see figure 15) There is still a cancellation between these two terms, but this is not as large as in the PV-dominated regime. The material rate of change of $\tilde{\zeta}'_z$ is of the same order of magnitude as in the PV-dominated regime, but now since $-2\nabla_h \cdot \boldsymbol{Q}_h$ is almost one order of magnitude smaller, this rate of change becomes important in the balance. There are three kinds of motion exhibited among the terms. First, $-2\nabla_h \cdot \boldsymbol{Q}_h$ and $-\tilde{\boldsymbol{\zeta}}'_h \cdot \nabla_h^2 \boldsymbol{u}_h$ show no wave motion at all, and the latter term is now negligible. Second, $\boldsymbol{u}_h \cdot \nabla_h \tilde{\zeta}'_z$, w_{zz}, $\tilde{\zeta}'_{zt}$ and $c^2 \nabla_h^2 w$ display wave motions with a period of about half the inertial period. Third, the terms $\tilde{\zeta}'_{zt}$ and $c^2 \nabla_h^2 w$ show also wave motions having shorter periods. Thus, the high frequency in the material rate of change of $\tilde{\zeta}'_z$ is due to the local rate of change, which is balanced by the high frequency change of

https://doi.org/10.1017/S0022112003004191 Published online by Cambridge University Press

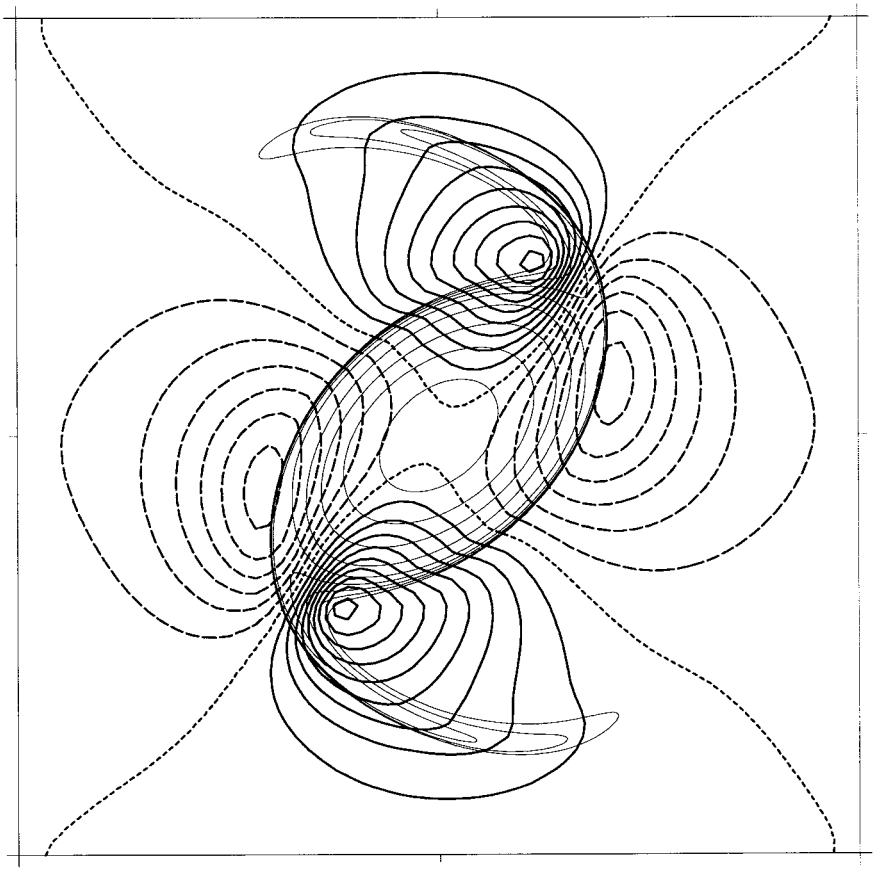


FIGURE 16. Horizontal distribution (as in figure 6) of w^q (thick lines, $\Delta = 1 \times 10^{-5}$) and PV contours (thin lines).

$c^2\nabla_h^2 w$. The high frequency in the material rate of change of $\tilde{\zeta}_z'$ is the residual of the cancellation between the local change $\tilde{\zeta}_{zt}'$ and the advective change $\boldsymbol{u}_h \cdot \nabla_h \tilde{\zeta}_z'$, and it is balanced by the high frequency change of w_{zz} and $c^2\nabla_h^2 w$, which add. Linear plane waves satisfy the balance $\tilde{\zeta}_{zt}' = c^2\nabla_h^2 w + w_{zz}$. This balance may be expected to hold only where the isopycnal displacement is sufficiently small (i.e. far from the main vortex). When the nonlinear term $\boldsymbol{u}_h \cdot \nabla_h \tilde{\zeta}_z'$ vanishes in figure 15 (this happens around $t = 18$ i.p.) the isopycnal displacement is large enough to contribute to $-2\nabla_h \cdot \boldsymbol{Q}_h$, and then the dominant balance is between this term and the three terms of the plane wave balance.

3.4.6. *Quasi-geostrophic vertical velocity*

The quasi-geostrophic vertical velocity w^q obtained solving (2.22) (figure 16) shows two main differences with respect to w (figure 7). The first is that w displays second-order internal gravity waves, not present in the smoother distribution w^q (internal gravity waves are filtered out in the QG approximation). The second is that the magnitude of w^q is usually smaller than that of w (see the scatter-plot of w^q versus w in figure 17). A linear fit using a 'robust' least-absolute-deviation method gives

https://doi.org/10.1017/S0022112003004191 Published online by Cambridge University Press

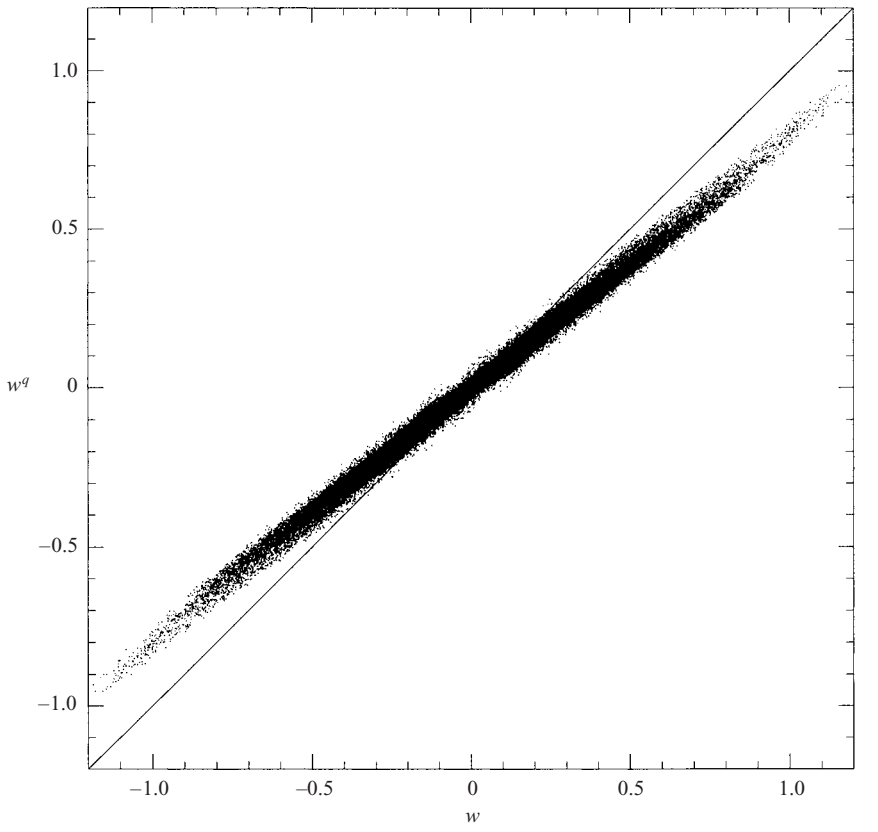


FIGURE 17. Scatter plot of w^q (y-axis) versus w (x-axis) at $t = 11$ i.p. (there are $64 \times 64 \times 128 = 524\,288$ points in the plot).

$w^q = 0.784w + [10^{-14}]$ (mean absolute deviation 0.75×10^{-2}) for the data shown in figure 17, meaning that w^q is about a 22% smaller than w. This difference depends on the magnitude of the PV anomaly. A second experiment, for a weaker anticyclonic gyre with a PV anomaly of $\varpi = -0.3$ at its centre, gave the relation $w^q = 0.898w + [10^{-15}]$. In this case w^q is only about a 10% smaller than w.

4. Concluding remarks

This work is a numerical analysis of the vertical velocity field in a single mesoscale baroclinic oceanic gyre. The evolution of the gyre during 20 inertial periods was simulated using a new three-dimensional numerical model which integrates the horizontal ageostrophic vorticity and explicitly conserves the PV via contour advection on isopycnal surfaces. A new initialization technique based on the slow, progressive growth of the PV field during an initial time interval was used to avoid the generation of internal gravity waves during the initialization of the gyre. The numerical balanced fields obtained were then used to carry out the first numerical analysis of the generalized ω-equation.

The use of the ageostrophic vorticity as a prognostic quantity, which is the Laplacian of a vector potential defining both the velocity and the density field, has been shown to be a powerful and feasible approach. This approach is combined with an

https://doi.org/10.1017/S0022112003004191 Published online by Cambridge University Press

explicit PV conservation method and the numerical inversion of a three-dimensional Monge–Ampère equation. In this framework the ω-equation is simply the horizontal divergence of the horizontal ageostrophic vorticity prognostic equation. Also, the PV initialization technique has been proven to be a very efficient one. It is able to generate a nearly balanced baroclinic gyre in which the influence of internal gravity waves in the mesoscale vertical velocity field is negligible. Internal gravity waves generated during the evolution of the gyre seem to be associated with vortex filamentation, but these waves are of second order in the vertical velocity field.

The numerical analysis of the generalized ω-equation has shown that, for moderately high Rossby numbers ($\varpi = -0.5$), the local and the advective rates of change of ζ_z' are of the same order of magnitude as the three largest terms in the ω-equation. There is, however, a large cancellation between these two terms, resulting in the approximate material conservation of ζ_z'. This might explain the over-applicability of the QG ω-equation for Rossby numbers larger than 0.1. It has been also shown that the term $-\tilde{\boldsymbol{\zeta}}_h' \cdot \nabla_h^2 \boldsymbol{u}_h$ is the fifth-most important one in the ω-equation. The terms $\tilde{\zeta} w_{zz}$ and $D_z \nabla_h^2 w$ are both of second order. The non-QG material rate of change of ζ_z', the fourth-most important term in the ω-equation, seems therefore to establish a limit for obtaining a diagnostic (time-independent) ω-equation that is more accurate than the QG ω-equation.

Future work along these lines might be directed toward the exploitation of the numerical approach in studying other geophysical flow phenomena. The success of the PV initialization method might also require further systematic study. And finally, further theoretical work is required to elucidate how the approximate material conservation of ζ_z' is related to the exact conservation of PV.

Support for this research has come from the UK National Environment Research Council (grant number GR3/11899), the Spanish program *Ramón y Cajal 2001* and the *Ministerio de Ciencia y Tecnología* (grant number REN2002-01343).

REFERENCES

Allen, J. T. & Smeed, D. A. 1996 Potential vorticity and vertical velocity at the Iceland-Færœs Front. *J. Phys. Oceanogr.* **26**, 2611–2634.

Allen, J. T., Smeed, D. A., Nurser, A. J. G., Zhang, J. W. & Rixen, M. 2001 Diagnosis of vertical velocities with the QG omega equation: an examination of the errors due to sampling strategy. *Deep-Sea Res.* I **48**, 315–346.

Davies-Jones, R. 1991 The frontogenetical forcing of secondary circulations. Part I: The duality and generalization of the Q vector. *J. Atmos. Sci.* **48**, 497–409.

Dritschel, D. G. 1998 On the persistence of non-axisymmetric vortices in inviscid two-dimensional flows. *J. Fluid Mech.* **371**, 141–155.

Dritschel, D. G. & Ambaum, M. H. P. 1997 A contour-advective semi-Lagrangian algorithm for the simulation of fine-scale conservative fields. *Q. J. R. Met. Soc.* **123**, 1097–1130.

Dritschel, D. G. & Viúdez, A. 2003 A balanced approach to modelling rotating stably stratified geophysical flows. *J. Fluid Mech.* (in press).

Haney, R. L. & Hale, R. A. 2001 The use of digital filter initialization to diagnose the mesoscale circulation and vertical motion in the California coastal transition zone. *J. Mar. Sys.* **29**, 335–363.

Holton, J. R. 1992 *An Introduction to Dynamic Meteorology*. Academic.

Hoskins, B. J. 1975 The geostrophic momentum approximation and the semi-geostrophic equations. *J. Atmos. Sci.* **32**, 233–242.

Hoskins, B. J. & Draghici, I. 1977 The forcing of ageostrophic motion according to the semi-geostrophic equations and in an isentropic coordinate model. *J. Atmos. Sci.* **34**, 1859–1867.

https://doi.org/10.1017/S0022112003004191 Published online by Cambridge University Press

Hoskins, B. J., Draghici, I. & Davies, H. C. 1978 A new look at the ω-equation. *Q. J. R. Met. Soc.* **104**, 31–38.

Krishnamurti, T. N. 1968 A study of a developing wave cyclone. *Mon. Wea. Rev.* **96**, 208–217.

Leach, H. 1987 The diagnosis of synoptic-scale vertical motion in the seasonal thermocline. *Deep-Sea Res.* **34**, 2005–2017.

Naveira Garabato, A. C., Allen, J. T., Leach, H., Strass, V. H. & Pollard, R. T. 2001 Mesoscale subduction at the Antarctic Polar Front Driven by Baroclinic Instability. *J. Phys. Oceanogr.* **31**, 2087–2107.

Panofsky, H. A. 1946 Methods of computing vertical motion in the atmosphere. *J. Met.* **3**, 45–49.

Pauley, P. M. & Nieman, S. J. 1992 A comparison of quasigeostrophic and nonquasigeostrophic vertical motions for a model-simulated rapidly intensifying marine extratropical cyclone. *Mon. Wea. Rev.* **120**, 1108–1134.

Pinot, J.-M., Tintoré, J. & Wang, D.-P. 1996 A study of the omega equation for diagnosing vertical motions at ocean fronts. *J. Mar. Res.* **54**, 239–259.

Pollard, R. T. & Regier, L. A. 1992 Vorticity and vertical circulation at an ocean front. *J. Phys. Oceanogr.* **22**, 609–625.

Räisänen, J. 1995 Factors affecting synoptic-scale vertical motions: a statistical study using a generalized omega equation. *J. Mar. Res.* **54**, 239–259.

Rudnik, D. L. 1996 Intensive surveys of the Azores Front. 2. Inferring the geostrophic and vertical velocity fields. *J. Geophys. Res.* **101**, 16291–16303.

Shearman, R. K., Barth, J. A. & Allen, J. S. 2000 Diagnosis of the three-dimensional circulation in mesoscale features with large Rossby number. *J. Phys. Oceanogr.* **30**, 2687–2709.

Strass, V. H. 1994 Mesoscale instability and upwelling. Part 2: Testing the diagnostics of vertical motion with a three-dimensional ocean front model. *J. Phys. Oceanogr.* **24**, 1759–1767.

Trenberth, K. E. 1978 On the interpretation of the diagnostic quasi-geostrophic omega equation. *Mon. Wea. Rev.* **106**, 131–137.

Viúdez, A. & Dritschel, D. G. 2002 An explicit potential vorticity conserving approach to modelling nonlinear internal gravity waves. *J. Fluid Mech.* **458**, 75–101.

Viúdez, A., Haney, R. L. & Tintoré, J. 1996*a* Circulation in the Alboran Sea as determined by quasi-synoptic hydrographic observations. Part II. Mesoscale ageostrophic motion diagnosed through density dynamical assimilation. *J. Phys. Oceanogr.* **26**, 706–724.

Viúdez, A., Tintoré, J. & Haney, R. L. 1996*b* About the nature of the generalized omega equation. *J. Atmos. Sci.* **53**, 787–795.

Viúdez, A., Tintoré, J. & Haney, R. L. 1996*c* Circulation in the Alboran Sea as determined by quasi-synoptic hydrographic observations. Part I. Three-dimensional structure of the two anticyclonic gyres. *J. Phys. Oceanogr.* **26**, 684–705.

Xu, Q. 1992 Ageostrophic pseudovorticity and geostrophic *C*-vector forcing – A new look at the *Q*-vector in three dimensions. *J. Atmos. Sci.* **49**, 981–990.

https://doi.org/10.1017/S0022112003004191 Published online by Cambridge University Press